LOOSE COUPLING OF SU2 MULTIPHYSICS CODE WITH PATO TO ANALYZE THE SURFACE RECESSION EFFECT ON SURFACE HEAT FLUX

A THESIS SUBMITTED TO
THE GRADUATE SCHOOL OF APPLIED MATHEMATICS
OF
MIDDLE EAST TECHNICAL UNIVERSITY

BY

MUTLU ÇELIK

IN PARTIAL FULFILLMENT OF THE REQUIREMENTS
FOR
THE DEGREE OF MASTER OF SCIENCE
IN
SCIENTIFIC COMPUTING

DECEMBER 2022

Approval of the thesis:

LOOSE COUPLING OF SU2 MULTIPHYSICS CODE WITH PATO TO ANALYZE THE SURFACE RECESSION EFFECT ON SURFACE HEAT FLUX

submitted by **MUTLU ÇELIK** in partial fulfillment of the requirements for the degree of **Master of Science in Scientific Computing Department, Middle East Technical University** by,

Prof. Dr. A. Sevtap Selçuk Kestel _____
Dean, Graduate School of **Applied Mathematics**

Assoc. Prof. Dr. Önder Türk _____
Head of Department, **Scientific Computing**

Prof. Dr. Ömür Uğur _____
Supervisor, **Scientific Computing, METU**

Prof. Dr. Sinan Eyi _____
Co-supervisor, **Aerospace Engineering Dept., METU**

Examining Committee Members:

Assoc. Prof. Dr. Nilay Sezer Uzol
Aerospace Engineering Department, METU _____

Prof. Dr. Ömür Uğur
Scientific Computing Department, METU _____

Assist. Prof. Dr. Sıtkı Uslu
Mechanical Engineering Department, TOBB _____

Date: _____

I hereby declare that all information in this document has been obtained and presented in accordance with academic rules and ethical conduct. I also declare that, as required by these rules and conduct, I have fully cited and referenced all material and results that are not original to this work.

Name, Last Name: MUTLU ÇELIK

Signature :

ABSTRACT

LOOSE COUPLING OF SU2 MULTIPHYSICS CODE WITH PATO TO ANALYZE THE SURFACE RECESSION EFFECT ON SURFACE HEAT FLUX

Çelik, Mutlu
M.S., Department of Scientific Computing
Supervisor : Prof. Dr. Ömür Uğur
Co-Supervisor : Prof. Dr. Sinan Eyi

December 2022, 57 pages

In this thesis, open source softwares SU2 Multiphysics and The Porous material Analysis Toolbox (PATO) based on OpenFOAM are used to conduct loosely coupled analysis of hypersonic non-equilibrium flow and thermochemical ablation. Both solvers have become prominent open source softwares with numerous validation and verification cases. NEMO, the non-equilibrium modeling solver of SU2 is used to model chemically reactive and non-equilibrium flows by integrating thermochemistry library of Mutation++. SU2-NEMO solves Navier Stokes equations with thermochemical non-equilibrium effects by using finite volume method.As a material response code, ablation solver PATO is used to calculate the surface temperature of solid materials and surface recession due to ablation. PATO, as a fully portable OpenFOAM library, discretizes conversation equations of total energy, gas momentum, gas mass, solid mass and gas species equations by finite volume method. The output of surface recession is used as input of SU2-NEMO for CFD analysis. SU2-NEMO then calculates the surface heat flux and pressure which are used as inputs of PATO. At the end, the effect of surface recession to surface heat flux distribution of blunt nose geometry is investigated.

Keywords: Ablation, Non-equilibrium flow, Hypersonic Aerothermodynamics

ÖZ

YÜZEY AŞINMASININ YÜZEY ISI AKISI ÜZERİNDEKİ ETKİSİNİ ANALİZ ETMEK İÇİN SU2 ÇOKLU FİZİK KODUNUN PATO İLE GEVŞEK BAĞLANTISI

Çelik, Mutlu
Yüksek Lisans, Bilimsel Hesaplama Bölümü
Tez Yöneticisi : Prof. Dr. Ömür Uğur
Ortak Tez Yöneticisi : Prof. Dr. Sinan Eyi

Aralık 2022, 57 sayfa

Bu tezde, OpenFOAM tabanlı The Porous material Analysis Toolbox (PATO) ve SU2 açık kaynak yazılımları, hipersonik denge dışı akış ve termokimyasal ablasyonun gevşek bağlanmış analizini yapmak için kullanılmıştır. Her iki çözücü de çok sayıda doğrulama vakasıyla öne çıkan açık kaynaklı yazılımlardır. SU2'nin denge dışı modelleme çözücüsü NEMO, Mutation++'ın termokimyasal kütüphanesini entegre ederek kimyasal olarak reaktif ve denge dışı akışları modellemek için kullanılmaktadır. SU2-NEMO, Navier Stokes denklemlerini termokimyasal denge dışı etkilerle sonlu hacim yöntemini kullanarak çözer. Malzeme tepki kodu olarak, ablasyon çözücüsü PATO, katı malzemelerin yüzey sıcaklığını ve ablasyon nedeniyle yüzey durgunluğunu hesaplamak için kullanılır. Tamamen taşınabilir bir OpenFOAM kütüphanesi olan PATO, enerji, momentum, gaz kütlesi, katı kütlesi ve gaz türleri denklemlerini sonlu hacim yöntemi ile ayrıklaştırır. Hesaplanan aşınma çıktısı, HAD analizi için SU2-NEMO'nun girdisi olarak kullanılmıştır. SU2-NEMO'nun daha sonra hesapladığı yüzey ısı akısı ve basıncı PATO'nun girdisi olarak kullanılmıştır. Küt burun geometrisinde yüzey çekilmesinin yüzey ısı akısı dağılımına etkisi incelenmiştir.

Anahtar Kelimeler: Ablasyon, Dengedışı akış, Ses ötesi Aerotermodinamik

ACKNOWLEDGMENTS

I would like to express my very great appreciation to my thesis supervisor Prof. Dr. Ömür Uğur and co-supervisor Prof. Dr. Sinan Eyi for their patient guidance, enthusiastic encouragement and valuable advices during the development and preparation of this thesis. Their willingness to give their time and to share their experiences has brightened my path.

Besides my advisors, I would like to thank the rest of my thesis committee members: Assoc. Prof. Dr. Sıtkı Uslu and Assoc. Prof. Dr. Nilay Sezer Uzol for their insightful comments. I would also offer my sincere thanks to Dr. Buğra Şimşek, Dr. Oğuz Kaan Onay and Dr. Kamil Özden for sharing their valuable experience with me.

I am also grateful to my fellow colleagues Berkan Yerlikaya and Sami Karabay for the stimulating discussions we had during this study. Additionally, this endeavor would not have been possible without the support from Roketsan Inc..

Final thanks to my dearest family. My supporting, caring and loving wife Duygu, it was a great comfort to know you were always there to encourage me. My lovely and kind parents Figen and Haldun, your precious belief in me were also so motivating during this difficult journey. My dear brother Mert, it was relief for me to know that I have a real brother on my back.

TABLE OF CONTENTS

LIST OF TABLES

LIST OF FIGURES

LIST OF ABBREVIATIONS

CFD	Computational Fluid Dynamics
FVM	Finite Volume Method
NEMO	Non-equilibrium Modeling
LeMANS	Michigan Aerothermodynamics Navier Stokes Solver
TPS	Thermal Protection System
FIAT	Fully Implicit Ablation and Thermal Response Program
PATO	Porous-Material Analysis Toolbox based on OpenFOAM
DPLR	Data-Parallel Line Relaxation Method for the Navier-Stokes Equations
AUSM	Advection Upstream Splitting Method

CHAPTER 1

INTRODUCTION

Thermal management has a significant role in design process of the high speed vehicles like aircrafts, space shuttles and missiles. To date, many different thermal protection systems (TPS) withstanding high aerothermal loads have been developed for them. One easy and efficient way is to use ablative TPS materials to dissipate high entering heat flux, which is a widely used heat shield for aircrafts. Therefore, modelling of ablation phenomenon and the physical environment of high speed flow is very important while deciding the feasibility of design from thermal point of view. This actually shows the need of conjugate analysis of high speed flow and thermal response of the ablative material.

Ablation simply means degradation or removing of a material surface due to chemical reactions, erosion or vaporization. There are mainly two classes of ablative materials: "charring" and "non-charring". Ablative material called as non-charring if the material does not have any chemical reaction during removal process(like a simple change of state), it is called as charred if high heat causes a chemical reaction inside the material which leads to leakage of pyrolysis gases. Mainly, charring ablative materials contain resin which decomposes and generates gas when heated adequately, this is an endothermic reaction which is called as "pyrolysis". This reaction starts from the upper part of material where thermal loads are present and when this reaction is done remaining material called as "char" or "charred material". If material does not reach necessary temperature for pyrolysis reactions, it is called as "virgin ablative material". The outflow gases ,which are produced during pyrolysis reactions, pass through porous structure of charred ablative material and behaves like a barrier against aerothermal heating(convective heating, radiative heating), this is another thermal protec-

tion effect of ablative materials. Lastly, during whole this process surface recession occurs due to mechanical erosion on charred part which causes a consistent decrease of material thickness. This general structure is shown on Figure 1.1 as shematic [26].

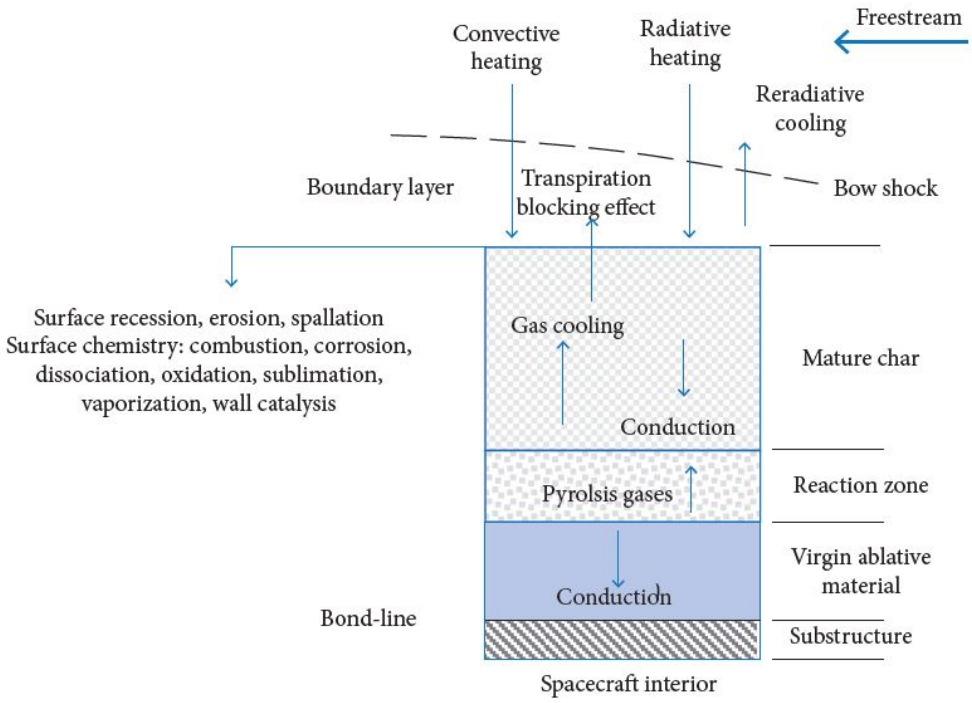

Figure 1.1: Shematic of charring ablative thermal protection system [26]

To accurately model the ablation, correct boundary conditions should be used. Therefore, precise modelling of high speed flow is needed to compute convective heat transfer on the ablating surface. The formation of a high temperature, strong shock layer in a flow field with mach number more than 5 causes the flow to sudden slow down and the gas' kinetic energy to be transformed into thermal energy, which is the primary cause of the high heat flux on the surface of the aerospace vehicle. Both molecule dissociation and ionization take place at high flow temperatures in the shock layer. Since they are the signs of thermal non-equilibrium, these events are referred to as non-equilibrium effects. Representation of a high enthalpy flow can be seen in Figure 1.2. Numerical modeling of the physics behind non-equilibrium flows is still a prime area in the aerospace society since the failure of NASA X-15 [39]. That catastrophe should be oft-sited case of non-equilibrium flow modelling since shock impingement

leaded a structural failure. Therefore, a CFD code which is capable of modeling non-equilibrium flow and coupling with an ablation solver to model surface recession is vital for high speed aerospace vehicle design.

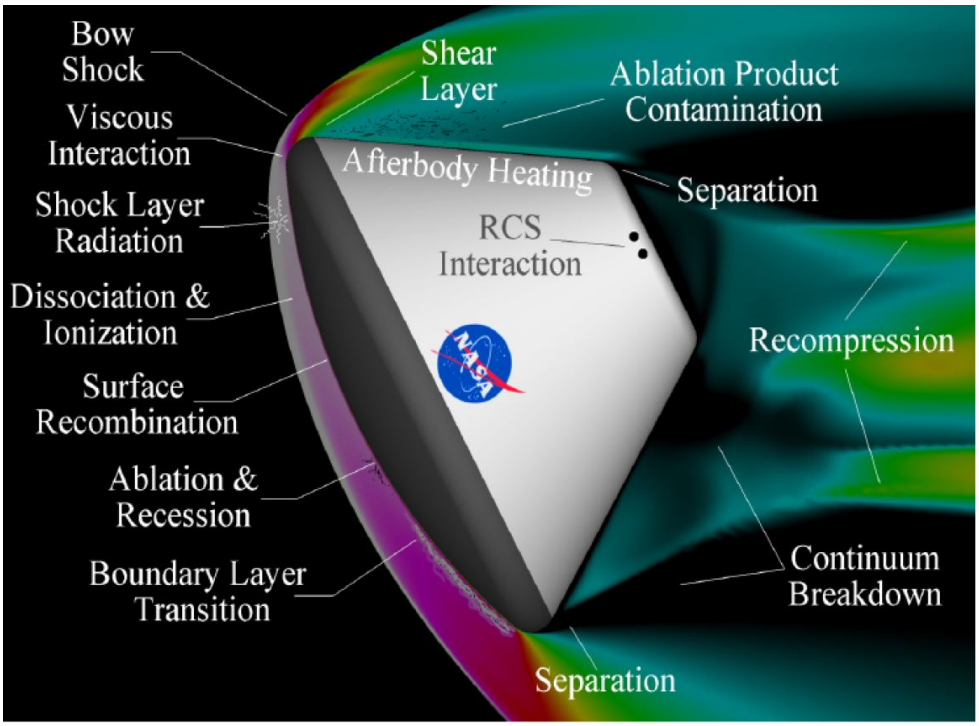

Figure 1.2: Shematic of non-equilibrium flow during the reentry of a blunt body [26]

1.1 Literature Review

Until 1950s no research was done about modeling or application of ablation phenomenon because there was no need for such a thermal protection system. Firstly, space engineers and researchers began thinking about how to return from space, especially from thermal point of view since atmospheric reentry is an important thermal challenge due to high heat loads. To overcome this challenge many different vehicle designs are tested through wind tunnels but just changing the design of the vehicle were not enough. Even though they could cope with thermal loads, weight increase became problem for trajectories due to using of high density metals such as copper as heat sink structure or using of very thick metal bodies. After that, first considerations have started about using ablative materials [2]. After necessary assessments and analysis done by researchers, using of ablative thermal protection system for at-

mospheric reentry became an important and logical choice due to its low density and high heat absorption properties. At this point, modelling of ablation became significant for scientists and engineers. In 1965, a significant Nasa Technical Note is published by Donald M. Curry which gives a detailed mathematical model for charring ablation thermal protection system [8]. He used 1D implicit finite difference method to formulate differential equations and developed a FORTRAN IV code to make necessary calculations. That paper also presented the verification of the model with experimental data. These mathematical model and its verification enable engineers to calculate minimum thickness required for the missions, this leads to using of ablative TPS for first successful controlled reentry mission of NASA [14](Gemini 6A, Figure 1.4) which is a manned reentry mission and then it is used in many space missions till today. In 1968, Charring Material Ablation (CMA) code published by Moyer and Rindall which is a industry standard 1D finite difference code. CMA is capable of modeling the pyrolysis reactions by using a non-cummulative method for the pyrolysis gas motion. It can be used for different types of charring ablators. There are many studies on the modeling of charring ablators available in the literature and a detailed review of them are demonstrated in Figure 1.3. In 1997, Fully Implicit Ablation and Thermal Response Program (FIAT) is developed and became the one of the most popular charring ablation modeler due to its numerical stability and robustness. It is a very well validated program and currently used by NASA. However, most of these models and simulation tools available in the literature are not free to access. Porous-Material Analysis Toolbox based on OpenFOAM (PATO) is the only prominent ablation model since it is an open source and free to access tool that can model the physics of the ablation with high fidelity. Detailed comparison of PATO and FIAT is done in [31]. There are also several studies for validation of PATO in the literature.

To model the ablation phenomenon correctly with the tools given in previous paragraph, surface pressure and convective heat flux values are needed as boundary conditions. This emphasizes the importance of a true computational model of hypersonic flow environment which gives the related boundary conditions as output. One of the first effort to model non-equilibrium flow with loosely coupled chemical source terms

Code capabilities Green : verified Yellow : under verification/to be released Red : in development	AMARYLLIS	CAMAC	CAT	CHALEUR	CHAP	CMA	CMAS	CMAK	COYOTTE2	FABL	FIAT	FIAT3D	HERO	ITRAC	LIBABLAT	MIG	MOPAR	NEQAP	NIDA	PATO	PRESENT	STAB	TITAN	TMU	US3D MOD
Summary																									
Model fidelity (1-3)	2	1	3	2	1	2	2	2	1	2	1	1	2	2	1	2	2	2	3	3	1	1	1	1	1
Code dimensionality (nD= 1-3)	3	1	1	1	1	1	1	1	3	1	1	3	3	1	1	1	1	1	1	3	1	1	2	1	1
Code maturity level (1-3)	3	1	2	2	2	3	3	3	2	2	3	2	2	3	1	1	2	1	1	2	2	3	3	2	1
Gas-phase Mass Conservation	In-depth : Eq. 1																								
Storage (∂_t ...)																									
Divergence (∂_x...)																									
Pyrolysis production (Π)																									
Pyrolysis model	In-depth: Eq. 2-7																								
SoA Arrhenius laws (-> Π)																									
Species production (-> πi)																									
Gas-species Conservation	In-depth: Eq. 8																								
Storage (∂t ...)																									
Divergence (∂x...)																									
Multi-component diffusion (∂xF)																									
Finite-rate chemistry (πi , ω_i)																									
Solid-phase mass conservation	In-depth: Eq. 9-10																								
Pyrolyzing matrix mass loss																									
In-depth ablation/coking																									
Momentum conservation	In-depth: Eq. 11																								
Darcy's law																									
Klinkenberg/Forchheimer																									
Energy conservation	In-depth: Eq. 12-13																								
Storage (∂t ...)																									
Divergence (∂x...)																									
Effective conduction																									
Viscous dissipation																									
Boundary conditions	At the wall: Eq. 14-22																								
Surface energy balance																									
Wall chemistry from B' table																									
Internal wall chemistry solver																									
Other utilities	Integrated libraries																								
Equilibrium chemistry solver																									
Integrated boundary layer code																									
Script -coupling to CFD code																									

Figure 1.3: List of Material Response Codes untill 2011 [19]

is done by Gnoffo and McCandless in 1986 [12]. By improving this work Gnoffo developed LAURA code in 1989 [13]. The solver uses separate conversation equation for each species. NASA Langley Research Center presented many validation studies of the LAURA solver. In 1998 Data-Parallel Line Relaxation Method for the Navier-Stokes Equations (DPLR) is developed by Wright, Candler and Bose in NASA Ames Research Center [40]. The blunt body vehicle's uniform shape is utilized by the DPLR solver for simulations on structured grids. Contrary to LAURA, DPLR uses a modified Gauss-Seidel line relaxation approach which exhibits quick convergence even in the presence of significant gradients. The main problem of DPLR is effectively creating of the structured grids, especially for complicated geometries. This

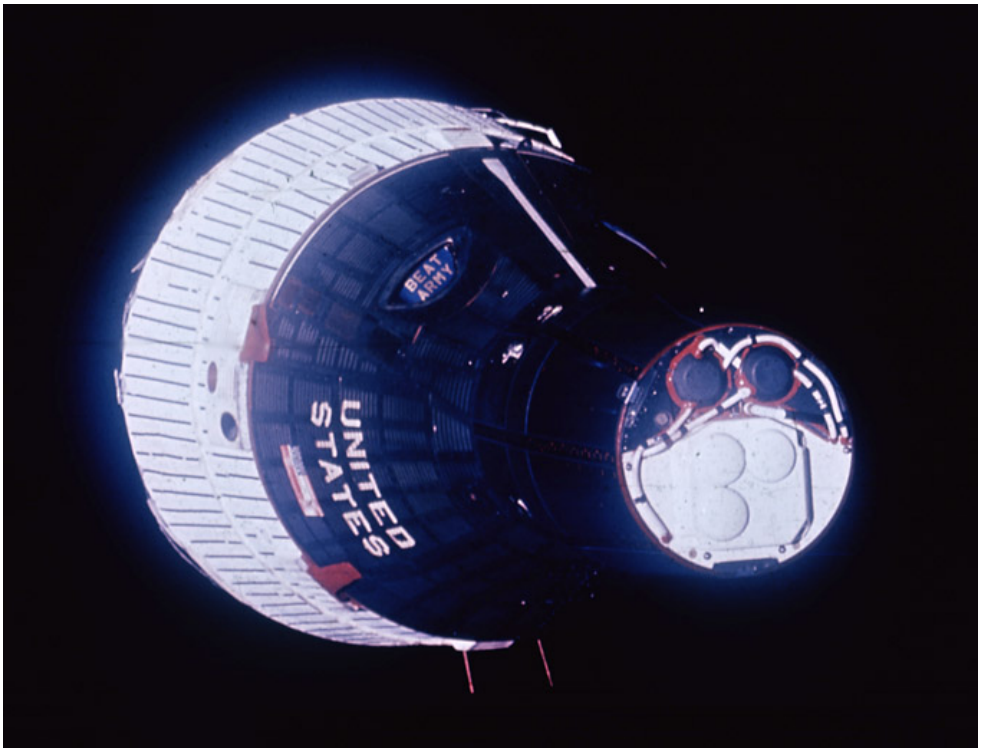

Figure 1.4: Gemini 6A spacecraft, black side is charring ablative TPS (painted)

issue is resolved in US3D which is an extension of the DPLR code in 2004 [30]. Beside the physical model of the non-equilibrium effects, US3D is capable of modeling the thermal response of the reactive material and shape change.

Up to this point, the non-equilibrium solvers explained here are inhouse codes and access and modification of them are not possible without permission. However with the recent efforts the number of open source solvers have increased. The three most used solvers are explained here. Firstly, in 2013 CoolFluid, an open source hypersonic reacting flow solver, is developed by Von Karman Institute of Fluid Dynamics and KU Leuven Center for mathematical Plasma Astrophysics [21]. CoolFluid is able to model space weather, aeroacoustic, turbulent and aerothermodynamic environment of different regimes, from incompressible to hypersonic. Secondly, OpenFOAM based solver hy2Foam is developed by taking the advantage of the two temperature model in 2015 [3]. Several validation cases of hy2Foam have been published and can be found in the literature. Lastly, SU2 NonEquilibrium MOdeling code has been developed recently as a solver of SU2 multiphysics code.With its design sensitivity, the SU2-NEMO algorithm stands as a noteworthy option for simulating hypersonic reacting flows [22]. Additionally, it is capable of employing a trustworthy external

thermochemical library: Multicomponent Thermodynamic and Transport properties for ionized gases library in C++(Mutation++) developed by Von Karman Institute for Fluid Dynamics [35]. Most of the open source CFD codes do not include a non-equilibrium model and the ones capable of solving thermodynamic non-equilibrium mostly have limited access such as LeMANS, US3D, LAURA and DPLR. On the other hand, CoolFluid, hy2Foam and SU2 are the open-source codes with unlimited access to model non-equilibrium flows.

In 1993, one of the first coupled analysis of ablation and hypersonic flow field with thermochemical non-equilibrium effects is performed by Keenan [16]. However, in that study pyrolysis gas leakage effect is not included. This deficiency was remedied by Bianchi in 2006 [2]. He conducted a fully coupled analysis with including a dynamic grid system deformation for two dimensional axisymmetric models. In the same period Amar introduced a high fidelity fully implicit tool that uses Darcy's law for the pyrolysis gas flow inside the charring zone [1]. In 2009, strongly coupling of LeMANS and self developed MOPAR codes is carried out by Martin and Boyd [24]. Hypersonic non-equilibrium flow is modeled by LeMANS and surface recession effect is included in MOPAR code in that study. Another study that couples LeMANS and MOPAR codes to simulate hypersonic ablation is again performed by Martin and Boyd where pyrolysis gases and dynamic mesh recession effects are introduced on the wall surface of the geometry and IRV-2 test vehicle's data is used to verify the coupled solution [25]. In 2016, a coupled fluid-ablation model for C/C composites under hypersonic non-equilibrium flow conditions is developed by using commercial softwares ANSYS Fluent and ABAQUS to simulate carbon ablation during Earth reentry [27]. Another coupled simulation work is done by Onay where self developed solvers for both ablation and hypersonic flow physics are used. There, the difference between coupled and decoupled simulation is investigated in detail [32].

1.2 Thesis Objectives

In the literature review section, the lack of open source ablation and non-equilibrium flow solvers coupling is noticed and there was no investigation of heat flux distribution change with the ablative surface recession by using open source software. There-

fore in this thesis study, loosely coupling of a recent developed open source non-equilibrium modeling solver, SU2-NEMO and open source tool for thermochemical ablation simulation, PATO is aimed to observe the effect of surface recession on heat flux distribution on a blunt body under hypersonic flow conditions. To achieve this coupling flow domain mesh needs to be automatically remeshed by using the surface recession data which is observed as a result of ablation analysis. Open source mesh software Salome is used for scripting and generating flow domain mesh. In structure part, there is no need for mesher since PATO does remeshing itself.

1.3 Thesis Plan

Theory of thermochemical ablation and physical modelling of material response tool PATO is explained in Chapter 2. Results of some validation cases are also given to show the tool's capabilities even though the corresponding validation cases are included in the test cases of the software. In Chapter 3, theoretical background of non-equilibrium flow, non-equilibrium flow modeling solver NEMO and the coupling methodology of ablation and non-equilibrium flow are explained in detail. In Chapter 4, verification and validation study of non-equilibrium flow model is stated with comparative results. Lastly, in graphite nose tip loosely coupled modeling and results chapter both flow field and material response results of graphite test specimen with its experimental results are shown. Chapter 5 ends with the conclusion and future work sections.

CHAPTER 2

THEORETICAL BACKGROUND OF ABLATION AND PATO

Ablative materials have been used in space missions with reentry as a primary thermal protection system alternative for decades. Decision of the thickness and the material of the ablative TPS is the essential point for thermal design engineers. Therefore, a well validated material response model of ablative material is needed. Porous material Analysis Toolbox based on OpenFOAM (PATO) has been developed as a high fidelity material response model to fulfil this need. PATO is a modular tool and OpenFOAM's adaptability and versatility are carried across to the tool. Even though any porous material might be modeled using PATO, the technology is now focused largely on porous ablative materials. The illustration of the porous ablative material's phenomenology is given in the Figure 2.1. It represents the model of carbon, phenolic material ablation in hypersonic flow aerothermal environment. PATO is responsible for the material response part and there are four different zones which can be classified by three seperate physicochemical phenomena:

- Thermochemical ablation take place in ablation zone where removing of the charred/coked material and surface recession occur. Ablation may result through chemical reactions such as oxidation($2\mathrm{C}_{(\mathrm{gr})} + \mathrm{O}_2 \leftrightharpoons 2\mathrm{CO}$ or nitridation, phase changes ($\mathrm{C}_{(\mathrm{gr})} \leftrightharpoons \mathrm{C}_{(\mathrm{gas})}$) , and even mechanical erosion/spallation depending on the aerothermal loads.

- In pyrolysis zone, thermal decomposition of the phenolic polymer causes carbonization of it to lower density carbon material. During pyrolysis reaction, hydrogen and phenol are produced which causes the mass losing of the material. This whole phenomena called as solid pyrolysis.

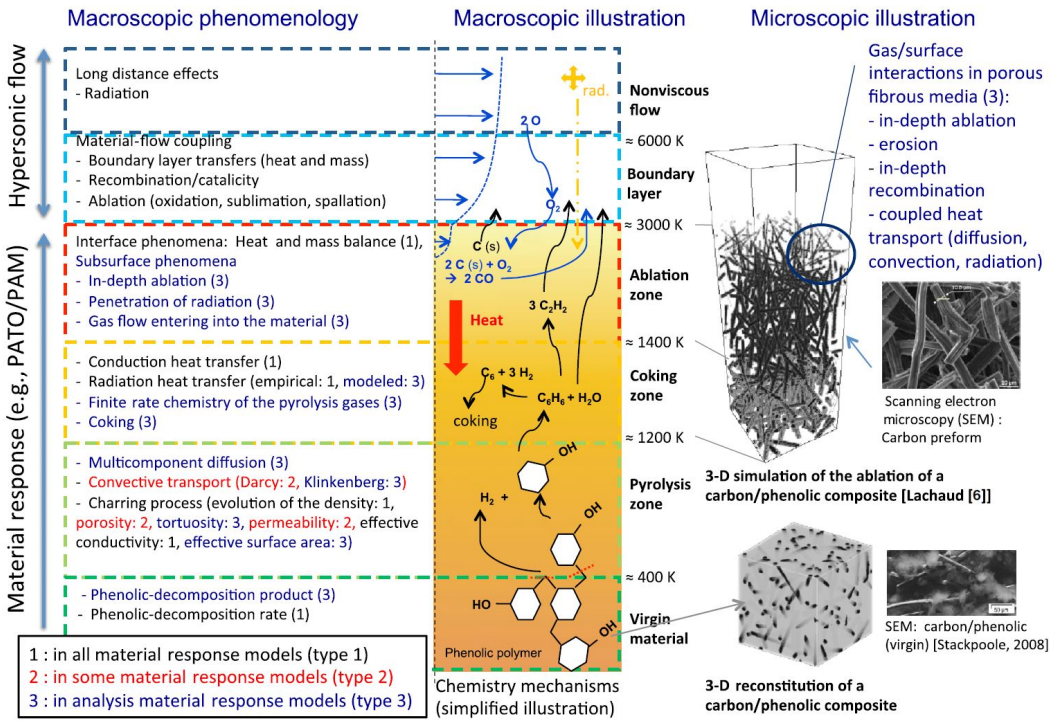

Figure 2.1: Shematic of non-equilibrium flow during the reentry of a blunt body[20]

- Throughout the pore network in the coking and ablation zones, the pyrolysis gases leak to the surface of the char. Chemical reactions occur both inside the pyrolysis gases(homogeneous, e.g., $C_6H_5OH + H_2 \leftrightharpoons C_6H_6 + H_2O$)) and between the char and the pyrolysis gases including probable coking impacts(heterogeneous, e.g., $C_6H_6 \leftrightharpoons C_{6(gr)} + 3H_2$)). Once boundary layer gases enter the porous ablation zone by forced convection or owing to rapid diffusion at high altitudes, the gases from the boundary layer may react or mix with the pyrolysis gases.

On the right side of the Figure 2.1 microscopic scale illustration is given. Numerical computation of that scale has a high cost in computational time. Even it is the real scale of the problem, there is a need for simplification to model it efficiently for thermal design applications. By using the method of volume averaging basic equations of microscopic scale can be modeled with physics based macroscopic equations. Modeling capabilities of the material response codes are categorized into three types in the Figure 2.1. PATO is able to model type 2 and type 3 phenomena on one, two or three dimensional models.

2.1 Governing Equations

In this part, the governing equations to model material response are introduced in volume averaged forms. For illustration purpose, low density carbon/phenolic is used as a sample so that Figure 2.1 can be used as guideline to understand the physics behind the mathematical equations. The equations mentioned below are explained following the work of Lachaud and Mansour [20].

2.1.1 Conservation of Mass

Amount of the pyrolysis gas produced is calculated through the conservation of mass equation 2.1.The time derivative term is neglected in type 1 and certain type 2 solvers. This assumption is valid when the changes in the important temperature and pressure, in comparison to the typical flow time in the porous media, are slow. The term Π indicates the produced pyrolysis gas and

$$\partial_t \left(\varepsilon_g \rho_g\right) + \partial_x \cdot \left(\varepsilon_g \rho_g \boldsymbol{v}_g\right) = \Pi \tag{2.1}$$

To find the average mass conservation equation, the direction of the gas velocity v_g, should be identified. This equation is numerically integrated in type 1 solvers under the presumption that the gas flow is oriented toward the surface and perpendicular to the surface. The direction and velocity of the flow must be established by solving the momentum conservation equation in different configurations. This is valid for one-dimensional (1-D) steady-state cases with an impermeable back face. A practical formula for $j \in [1, N_p]$ pyrolysis processes for any pyrolyzing phase inside of a specific ablative material is

$$\mathrm{PM}_j \rightarrow \sum_{i=1}^{N_g} \gamma_{ji} A_i \tag{2.2}$$

Here PM_j is fictive solid species of the pyrolyzing substance, that is the phenolic matrix in the case of low-density carbon/phenolic. Given by is the pyrolyzing phase density

$$\varepsilon_m \rho_m = \varepsilon_{mv} \rho_{mv} \sum_{j=1}^{N_p} F_j \left(1 - \xi_j\right) \tag{2.3}$$

where

$$\frac{\partial_t E_j}{(1-\xi_j)^{m_j}} = T^{n_j}\mathcal{A}_j \exp\left(-\frac{E_j}{\mathcal{R}T}\right) \tag{2.4}$$

The source of pyrolysis gas is

$$\Pi = -\partial_t\left(\varepsilon_m \rho_m\right) = \varepsilon_{\mathrm{mv}}\rho_{\mathrm{mv}} \sum_{j=1}^{N_p} F_j \partial_t\left(\xi_j\right) \tag{2.5}$$

Although the equations used in the literature to describe pyrolysis have many forms, they are all mathematically comparable. Modern design codes of type 1 and type 2 do not monitor species production. The pyrolysis gas's elemental fraction is considered to be constant. This is known to not be entirely accurate because the gases produced during pyrolysis do not always have the same composition. Chemical equilibrium is assumed while computing the chemical composition of the gas and the derived values (i.e. gas enthalpy).In case of a leading model that is exothermic rather endothermic, due to the true gas composition is unknown, additional parameters (such as viscosity, mean molar mass, and diffusion coefficients) are also uncertain.

It is crucial to empirically determine the molar composition of the pyrolysis gases in addition to their elemental content for high-fidelity modeling. The following formula is used to calculate the rate of pyrolysis gas production for each species i

$$\pi_i = \epsilon_m \rho_{\mathrm{mv}} \sum_{j=1}^{N_p} \left[\partial_t \xi_j F_j \tilde{\gamma}_{ji}\right] \tag{2.6}$$

where

$$\tilde{\gamma}_{ji} = \frac{\gamma_{ji}}{\sum_{k=1}^{N_g} \gamma_{jk}\mathcal{M}_k} \tag{2.7}$$

The stoichiometric factors γ_{ji} should be experimentally determined because they are not readily available in the literature. The total pyrolysis gas output for types 1 and 2 solvers can still be calculated from the same set of data by adding up the production terms $\Pi = \sum_{i=1}^{N_s}\left[\pi_i M_i\right]$. Clearly, some quality data is missing throughout the aggregating process, but this effectively illustrates how type 1, 2, and 3 models are all compatible with one another and how code users can always switch back to the most basic models while in possession of type 3 data. In order to precisely follow species

mobility and chemical reactions within the material's pores, type 3 models incorporate the species conservation equation. One way to express the species conservation equation in mass fraction y_i is as follows

$$\partial_t \left(\epsilon_g \rho_g y_i\right) + \partial_x \cdot \left(\epsilon_g \rho_g y_i v_g\right) + \partial_x \cdot \mathcal{F}_i = \pi_i M_i + \epsilon_g \omega_i M_i \tag{2.8}$$

where $\mathcal{F}_i$ is the diffusion flux of the i th species. We approach the challenging topic of multicomponent mass transfer in porous media in two ways. The average bulk diffusion coefficients for each species are estimated first. The effects of tortuosity in all regimes are then taken into consideration in a second stage using the Bosanquet model [18] (Knudsen to continuum). All models incorporate a solid phase mass conservation model to determine the solid's actual density. Modeling of the matrix's volume-averaged density change as a result of pyrolysis Π uses forms equal to

$$\partial_t \left(\epsilon_m \rho_m\right) = -\Pi \tag{2.9}$$

In type 1 and type 2 codes, coking is entirely eliminated. Since ablation and spallation are treated as surface phenomena, in-depth equations do not include them. The solid mass conservation equation is expanded in the proposed type 3 framework to take into consideration in-depth heterogeneous processes, and spallation

$$\partial_t \left(\epsilon_s \rho_s\right) = \partial_t \left(\epsilon_m \rho_m + \epsilon_f \rho_f\right) = -\Pi + \sum_{i \in s} \epsilon_g \omega_i M_i + \sum_{i \in s} \tau_i M_i \tag{2.10}$$

For any element, this general mass balance is accurate. Finding the intrinsic heterogeneous response rates for coking $\omega_{i,i \in s}$ and ablation is a difficult issue. The in-depth ablation and coking behaviors of the different phases depend on the microstructure of the material of interest.

2.1.2 Conservation of Momentum

By solving the momentum conservation equation, the average gas velocity is determined. The volume-averaged momentum conservation in porous media structure can be expressed as:

$$v_g = -\frac{1}{\varepsilon_g \mu} \frac{1 + \beta/p}{1 + Fo} \underline{\underline{\boldsymbol{K}}} \cdot \partial_x p \tag{2.11}$$

Due to the anisotropy of the majority of the materials, the permeability $\underline{\underline{\boldsymbol{K}}}$ is a second-order tensor. Orthotropic permeability characteristics, for instance, can be found in FiberForm, the carbon preform of the Phenolic Impregrated Carbon Ablator (PICA) [23]. Momentum conservation transforms into Darcy's rule ($\beta = 0$, $Fo = 0$) for approaching Stokes flows in the continuum regime (in the material's pores). The Klinkenberg correction, denoted by the phrase $1 + \beta/p$, takes slip effects at the pore scale into account when the Knudsen number is not low, and the Knudsen number is the ratio of the mean free path to the mean pore diameter. Forchheimer correction, repsented by $1 + Fo$, is for accounting high-Mach impacts at pore scope (ongoing regime's flow pattern). Forchheimer effects are often anticipated in dense ablative materials exposed to extremely high heat fluxes and pyrolysis gas speeds more than 50 m/s. Utilizing both corrections at once is not recommended because they address separate regimes.

2.1.3 Conservation of Energy

Gas and solid forms are in equilibrium thermal state, in accordance with Puiroux et al. [34], as long as the Péclet number for thermal conduction within pores is low ($Pe = \epsilon_g \rho_g c_{p,g} d_p v_g / k_g$). The low pore size ($< 100\mu\mathrm{m}$) and slow pyrolysis flow of gas ($v_g \sim 1\ \mathrm{m/s}$) in the majority of cases of interest to space agencies assure a low Peclet number because the gas temperature adjusts to the solid temperature inside the pores [18]. The condition of thermal equilibrium allows us to express the conservation of energy as:

$$\begin{aligned} &\partial_t \left(\rho_a e_a\right) + \partial_x \cdot \left(\epsilon_g \rho_g h_g \boldsymbol{v}_g\right) + \partial_x \cdot \sum_{i=1}^{N_g} \left(h_i \mathcal{F}_i\right) \\ &= \partial_x \cdot \left(\underline{\underline{k}} \cdot \partial_x T\right) + \mu \varepsilon_g^2 \left(\underline{\underline{\boldsymbol{K}}}^{-1} \cdot \boldsymbol{v}\right) \cdot \boldsymbol{v} \end{aligned} \tag{2.12}$$

where the ablative material's total stored energy equals the energy of all of its phases

$$\rho_a e_a = \epsilon_g \rho_g e_g + \epsilon_m \rho_m h_m + \epsilon_f \rho_f h_f \tag{2.13}$$

The second and third variables on the left-hand side of the equation are, respectively, the energy that the pyrolysis gases convect (advection) and transmit (diffusion). The Fourier's law is a straightforward way to model heat transfer as an efficient diffusive transport. A second-order tensor called the effective conductivity, or $\underline{\mathbf{k}}$, accounts

for functional radiative heat transfer as well as conduction in solids and gases. This strategy's efficacy is debatable. The key problem is whether or not the radiative heat transfer can be linearized. Radiative heat transport for two-dimensional (2-D) carbon fiber preforms has been demonstrated to be linearizable in a theoretical research [36, 37]. The experimental validation and applicability to various materials are not simple and require investigation; however, this is outside the scope of this paper. The energy lost due to viscous effects in the Darcian regime is represented by the second term on the right [10]. Usually, it is negligible in comparison to the heat transfer term. It may appear that type 3 models do not significantly improve the momentum and energy conservation equations. However, because the following quantities are now calculated with greater accuracy: viscosity, average molar mass, porosity, permeability, and enthalpies, they effectively inherit the detailed resolution of the mass conservation equations.

2.1.4 Surface Energy Balance

Surface energy balance has a significant role in this study since it gives the net energy on the surface of the geometry which is the net heat flux in the current thesis.

$$q_{\text{conv}} - (\rho V)h_w + q_{\text{rad,in}} - q_{\text{rad,out}} - q_{\text{cond}} + \dot{m}_{\text{pg}}h_{\text{pg}} + \dot{m}_{\text{ca}}h_{\text{ca}} = 0 \qquad (2.14)$$

Here, the terms from left to right are: convective heat flux, advective flux, radiative heating, radiative cooling, pyrolysis gas flux and char ablation flux. The convective heat flux $[q_{\text{conv}} = \rho_e u_e C'_H (h_e - h_w)]$ and the radiative heat flux are extracted from CFD simulations.To account for the obstacle caused by the pyrolysis-ablation gas blowing, the heat transfer Stanton number C_H is revised, which also adjusts the heat transfer coefficient. For instance, the following adjustment is commonly implemented, a dimensionless mass flow rate is B' which is defined as: $C'_H = C_H \ln(1 + 2\lambda B') / \ln(2\lambda B')$, $B' = (\dot{m}_{\text{pg}} + \dot{m}_{\text{ca}}) / (\rho_e u_e C_M)$ where λ is a multiplier to scale down, usually taken as 0.5 for laminar flows [6] and C_M is the mass transfer Stanton number.

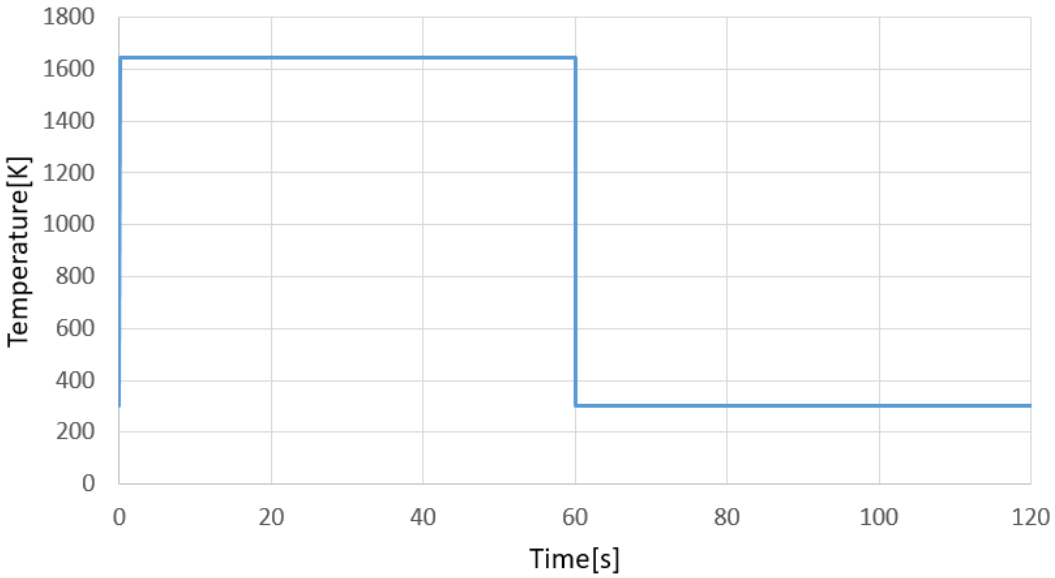

Figure 2.2: Temperature Boundary Condition of The Test Case

2.2 1D Test Case for Verification

To able to see the solver capabilities, a basic test case of Ablation Test Case 1.0 tutorial of the solver is studied. It is a transient analysis with total time of 120 seconds. Since it is a 1D model, mesh is generated by using OpenFOAM's "blockmesh" option. In total 50 elements are used. Two boundary conditions are defined on the top of the rod: time dependent temperature(given in Figure 2.2), constant pressure 101325 Pa. Initially, all elements are defined with 300 kg/m^3 density. The material is an experimental material of TACOT which is exist in the library of Mutation++ with the all necessary thermochemical properties.

First 60 seconds thermochemical ablation with pyrolysis reactions is modeled and for the last 60 seconds only conduction equation is solved. Results are compared with the FIAT code results which were available in the test case folders. As it is clearly seen in Figures 2.3 and 2.4, the temperature and pyrolysis gases mass production results of PATO and FIAT are agreed well. TC represents thermocouple and from 7 different points transient temperature data is saved to make the comparison. To make the surface temperature magnitude clear, it is showed separately with the black line with 'Wall' legend. Dashed lines are FIAT results but since the results' difference is around 2% it is barely visible. This study is conducted just to observe the verification of the ablation modeling tool PATO.

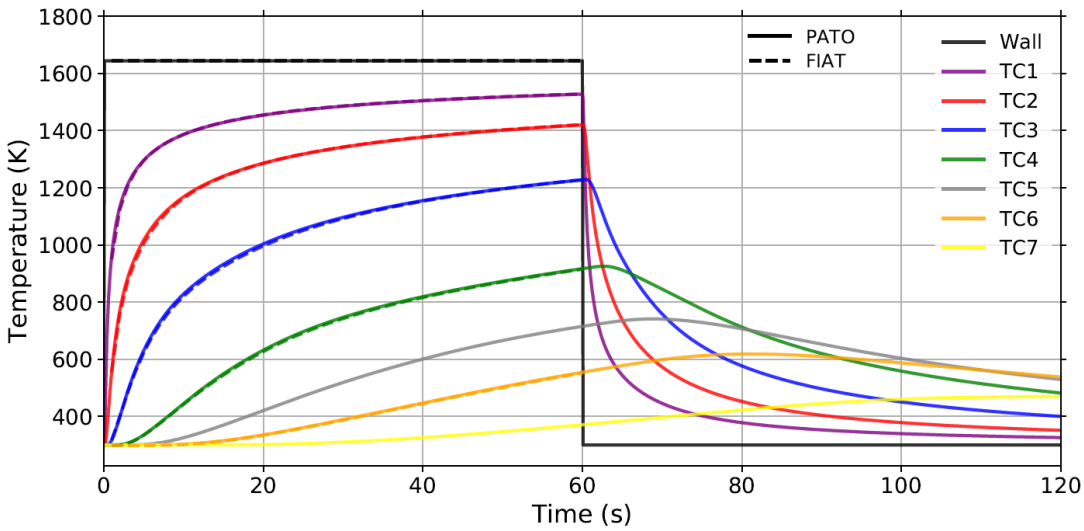

Figure 2.3: Comparison of Temperature Results

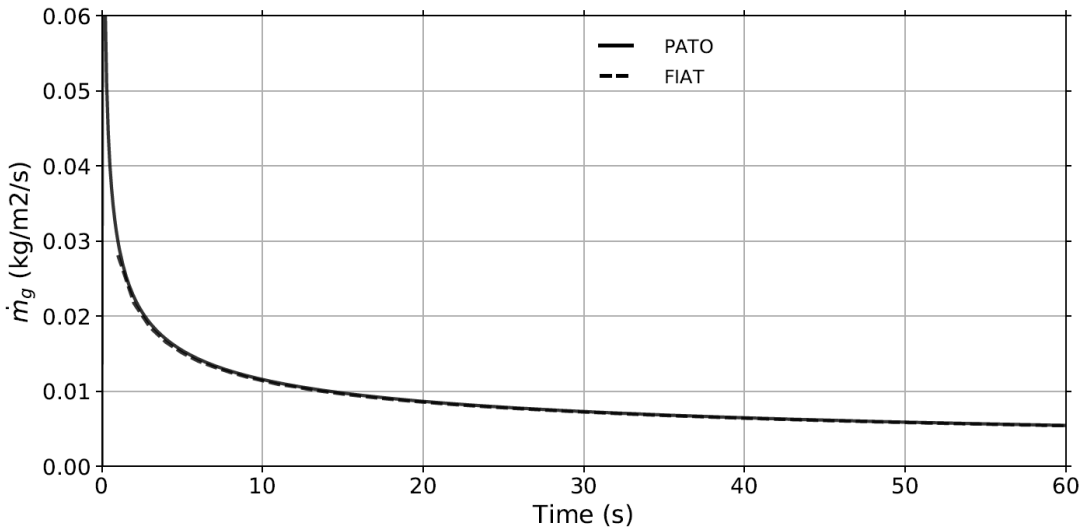

Figure 2.4: Comparison of Pyrolysis Gas Mass Production Rate Results

CHAPTER 3

THEORETICAL BACKGROUND OF SU2 NON-EQULIBRIUM MODELING SOLVER AND COUPLING METHODOLOGY

SU2 NonEquilibrium MOdeling (NEMO) [1] solver, which is the recent enhanced version of SU2 Multiphysics software to model reacting flows in thermochemical nonequilibrium. The solver is coupled with Mutation++ (Multicomponent Thermodynamic and Transport properties for IONized gases in $\mathrm{C++}$) library that provides the needed thermochemical properties of the air and carbon dioxide mixture chemistry models.

SU2-NEMO is capable of importing two thermochemical libraries: Mutation++ and SU2 Native Thermochemical Library. Mutation++ is a well validated library that can simulate wide range of gas mixtures efficiently. Although, SU2 Native Thermochemical Library is developed for SU2-NEMO, previous studies show that Mutation++ is computationally much more efficient[1]. So that in present study SU2-NEMO is coupled with Mutation++.

3.1 Governing Equations

SU2-NEMO solves the partial differential equations of Navier Stokes equations with non-equilibrium effects given by Equation 3.1 below. Here F^c and F^v represent convective flux and viscous flux respectively. For inviscid flow, F^v term is ignored. U is the conservative variables which are given after the equation and Q is the source

term.

$$R(U, \nabla U) = \frac{\partial U}{\partial t} + \nabla \cdot F^c(U) - \nabla \cdot F^v(U, \nabla U) - Q(U) = 0 \tag{3.1}$$

where,

$$U = \begin{Bmatrix} \rho_1 \\ \vdots \\ \rho_{n_s} \\ \rho \boldsymbol{u} \\ \rho e \\ \rho e^{ve} \end{Bmatrix}, \quad F^c = \begin{Bmatrix} \rho_1 \boldsymbol{u} \\ \vdots \\ \rho_{n_s} \boldsymbol{u} \\ \rho \boldsymbol{u}\boldsymbol{u}^T + PI \\ \rho h \boldsymbol{u} \\ \rho e^{ve} \boldsymbol{u} \end{Bmatrix}$$

$$F^v = \begin{Bmatrix} -\boldsymbol{J}_1 \\ \vdots \\ -\boldsymbol{J}_{n_s} \\ \sigma \\ \boldsymbol{a}^T \sigma - \sum_k - \sum_s \boldsymbol{J}_s h_s \\ -q^{ve} - \sum_s J_s e^{ve} \end{Bmatrix}, \quad Q = \begin{Bmatrix} \dot{\omega}_1 \\ \vdots \\ \dot{\omega}_{n_s} \\ \boldsymbol{0} \\ 0 \\ \dot{\Theta}^{tr:ve} + \sum_s \dot{\omega}_s e_s^{ve} \end{Bmatrix}$$

In conservative variables vector U, ρ_i is the density of the ith species, u is the velocity, e is the total energy and e^{ve} is the vibrational energy . In convective fluxes terms, h represents the total enthalpy of the unit mass and P is the total pressure of the mixture. Viscous terms begin with $\boldsymbol{J}$ which is the mass diffusion flux of the species, and it is computed with Fick's law of diffusion, notation of n_s indicates the number of species and D_s is the multicomponent diffusion coefficient.

Lastly, viscous stress tensor σ and the heat conduction by using Fourier's law are given by:

$$\boldsymbol{\sigma} = \boldsymbol{\mu} \left(\boldsymbol{\nabla u} + \boldsymbol{\nabla u}^T - \frac{2}{3} \boldsymbol{I} (\boldsymbol{\nabla} \cdot \boldsymbol{u}) \right), \tag{3.2}$$

$$\boldsymbol{q}^k = \lambda^k \nabla \left(T^k \right), \tag{3.3}$$

where λ^k is the thermal conductivity of the kth energy mode and T^k is the temperature of the kth energy mode. For the thermal conductivity calculation vibrational and translational temperatures should be considered together so that Eucken's formula is used.

First source terms are the volumetric mass production rates of thermochemical reactions. For the reaction r the equation is:

$$\dot{\omega} = M_s \sum_r \left(\beta_{s,r} - \alpha_{s,r}\right)\left(R_r^f - R_r^b\right), \tag{3.4}$$

where

$$\begin{aligned} R_r^f &= k_r^f \prod_s \left(\frac{\rho_s}{M_s}\right)^{\alpha_{s,r}}, \\ R_r^b &= k_r^b \prod_s \left(\frac{\rho_s}{M_s}\right)^{\beta_{s,r}}. \end{aligned} \tag{3.5}$$

where R^f and R^b gives the reaction rates of forward and backward reactions. The coefficients of k_r^f and k_r^b give the reaction rate by Arrhenius equation which computes the reaction rate coefficients through experimental constants such as activation energy(ϵ_r), empirical exponent(η_r) and factor C_r. The coefficients of $\alpha_{s,r}$ and $\beta_{s,r}$ also come from the reaction nature. SU2-NEMO uses Park [33] curve fit to determine these constants. Arrhenius equation is computed by the following equation:

$$k_r^f = C_r \left(T_r\right)^{\eta_r} \exp\left(-\frac{\epsilon_r}{k_B T_r}\right) \tag{3.6}$$

The reaction's rate controlling temperature (T_r) is obtained by the following equation which is essentially the geometric average of the two temperature modes.

$$T_r = (T)^{a_r} \left(T^{ve}\right)^{b_r} \tag{3.7}$$

a_r and b_r are coming from the reaction's nature and depending on being forward or backward reaction their values change. For instance, in a dissociation reaction ($\mathrm{AB} + \mathrm{M} \rightleftharpoons \mathrm{A} + \mathrm{B} + \mathrm{M}$) for forward reaction rate, it equals to $T_\mathrm{c} = \sqrt{T_\mathrm{tr} T_\mathrm{ve}}$ but for backward reaction rate it becomes $T_\mathrm{c} = T_\mathrm{tr}$.

3.1.1 Two Temperature Model

The set of governing equations that characterizes hypersonic flows must be closed by computing the source terms and non-equilibrium thermodynamic state. By integrating with the necessary multi-temperature thermochemistry libraries, this is accomplished. In current study Mutation++ is used since it provides the two temperature model for different gas mixtures which is explained in the next paragraph in detail.

Each species of the gas mixture is approximated as ideal gas so that Dalton's Law is used to calculate the total pressure of the mixture with equation 3.8

$$p = \sum_{s=1}^{n_{\mathrm{S}}} p_s = \sum_{s=1}^{n_{\mathrm{s}}} \rho_s \frac{R_{\mathrm{u}}}{M_s} T_{\mathrm{tr}} \tag{3.8}$$

With a similar approach total specific energy of the mixture is calculated as the summation of the kinetic energy and the internal energy of the each species.

$$e = \sum_{s=1}^{n_{\mathrm{s}}} c_s e_s + \frac{1}{2} u^2, \tag{3.9}$$

Multiplication of mass fraction (c_s and specific energy (e_s) of the species, which is the sum of every internal energy mode given in equation 3.10, gives the internal energy of each species in the equation 3.9.

$$e_s = e_s^{\mathrm{t}}\left(T_{\mathrm{tr}}\right) + e_s^{\mathrm{r}}\left(T_{\mathrm{tr}}\right) + e_s^{\mathrm{v}}\left(T_{\mathrm{ve}}\right) + e_s^{\mathrm{e}}\left(T_{\mathrm{ve}}\right) + e_s^{0}. \tag{3.10}$$

In the modeling of non-equilibrium effects, air species are considered as polyatomic molecules and energy of these molecules are defined in five forms as vibrational, electronic, translational, and rotational. Each energy mode has a relation with other energy modes, but it is very complex to model all these interactions with CFD. Therefore, SU2-NEMO uses two temperature model which assumes translational (e_s^t) rotational (e_s^{r}) energy modes are in equilibrium as well as vibrational (e_s^v) and electronic (e_s^e) energy modes for each species s. However, these two couples do not need to be in equilibrium. Under this approximation the total energy and vibrational-electronic (e^{ve}) energy is calculated with :

$$\rho e = \sum_s \rho_s \left(e_s^t + e_s^r + e_s^v + e_s^e + e_s^o + \frac{1}{2} \boldsymbol{u}^T \boldsymbol{u} \right), \tag{3.11}$$

$$\rho e^{ve} = \sum_s \rho_s \left(e_s^v + e_s^e \right). \tag{3.12}$$

The term e_s^o gives the formation energy of the species at $298.15\ \mathrm{K}$ temperature and of $1\ \mathrm{atm}$ pressure. For the other energy modes, storing energies are calculated by using:

$$e_s^{\mathrm{t}}\left(T_{\mathrm{tr}}\right) = \begin{cases} \frac{3}{2} \frac{R_{\mathrm{u}}}{M_s} T_{\mathrm{tr}}, & \text{for linear molecules and atoms,} \\ 0, & \text{for electrons,} \end{cases} \tag{3.13}$$

$$e_s^{\mathrm{r}}\left(T_{\mathrm{tr}}\right)=\begin{cases}\frac{R_{\mathrm{u}}}{M_s}T_{\mathrm{tr}}, & \text{for linear molecules,}\\ 0, & \text{for atoms and electrons,}\end{cases} \tag{3.14}$$

$$e_s^{\mathrm{v}}\left(T_{\mathrm{ve}}\right)=\begin{cases}\frac{R_{\mathrm{u}}}{M_s}\sum_v \frac{\theta_{v,s}^{\mathrm{v}}}{\exp\left(\theta_{v,s}^{\mathrm{v}}/T_{\mathrm{ve}}\right)-1}, & \text{for molecules}\\ 0, & \text{for atoms and electrons}\end{cases} \tag{3.15}$$

$$e_s^{\mathrm{e}}\left(T_{\mathrm{ve}}\right)=\begin{cases}\frac{R_{\mathrm{u}}}{M_s}\frac{\sum_i g_{i,s}\theta_{i,s}^{\mathrm{e}}\exp\left(-\theta_{i,s}^{\mathrm{e}}/T_{\mathrm{ve}}\right)}{\sum_i g_{i,s}\exp\left(-\theta_{i,s}^{\mathrm{e}}/T_{\mathrm{ve}}\right)}, & \text{for molecules and atoms}\\ 0, & \text{for electrons}\end{cases} \tag{3.16}$$

In the last row of the source vector Q given in Section 3.1., the term $\dot{\Theta}^{\mathrm{tr:ve}}$ stands for vibrational relaxation and Landau-Teller($\langle\tau_s\rangle_{L-T}$) relaxation time with Park high temperature correction(τ_{ps}) is used for computing it which is given in Equation 3.17-3.19. correction.

$$\dot{\Theta}^{tr:ve}=\sum_S \rho_S\frac{de_S^{ve}}{dt}=\sum_S \rho_S\frac{e_S^{ve*}-e_S^{ve}}{\tau_S}, \tag{3.17}$$

where

$$\tau_s=\langle\tau_s\rangle_{L-T}+\tau_{ps}, \tag{3.18}$$

$$\langle\tau_s\rangle_{L-T}=\frac{\sum_r X_r}{\sum_r X_r/\tau_{sr}}. \tag{3.19}$$

The term τ_s is the relaxation time of specie s. It is computed by using the empirical formula of Millikan and White [28] with Park correction

$$\tau_{s-r}^{\mathrm{MW}}=\exp\left(A_{s,r}\left(T^{-\frac{1}{3}}-B_{s,r}\right)-18.42\right)\left(\frac{p}{101325}\right)^{-1}[\,\mathrm{s}], \tag{3.20}$$

and the Park correction:

$$\tau_s^{\mathrm{P}}=\left(N_s\sigma_s\sqrt{\frac{8R_{\mathrm{u}}T_{\mathrm{tr}}}{\pi M_s}}\right)^{-1}. \tag{3.21}$$

3.2 Numerical Model

In this section, the numerical deployment of models inside SU2-NEMO is highlighted. This covers both time-integration techniques and the discretization of the governing equations. The convective schemes used by SU2-NEMO, which are more specifically adapted to high speed flows, are discussed in more depth rather than explaining whole basic SU2 numerical procedures that related information may be found in [9].The discretized system of equations on an edge based median dual grid mesh are solved by SU2 using the Finite Volume Method. For a control volume Ω_i, the discretized equations can be formulated as:

$$0 = \int_{\Omega_i} \frac{\partial \mathbf{U}_i}{\partial t} d\Omega + \sum_{j \in N(i)} \left(\hat{\mathbf{F}}^c_{ij} + \hat{\mathbf{F}}^v_{ij} \right) \Delta S_{ij} - \mathbf{Q} \left| \Omega_i \right| = \int_{\Omega_i} \frac{\partial \mathbf{U}_i}{\partial t} d\Omega + \mathbf{R} \left(\mathbf{U}_i \right) \tag{3.22}$$

In the equation, N(i) represents the neighbour nodes of ith node and ΔS_{ij}. Computations of the fluxes are made at the midpoint of each edge and each of the two nodes form an edge by adding residual ($\mathbf{R} \left(\mathbf{U}_i \right)$) to fluxes.

3.2.1 Convective Flux

SU2-NEMO is capable of implementing upwind and central convective schemes that standard SU2 can. Instead of expaining every scheme, only Advection Upstream Splitting Method(AUSM) is explained in this study since it is used as convective scheme of the model. It is a NEMO specific flux splitting method of SU2 which is mainly implemented in high speed flow models. Approximated flux of AUSM scheme is given as:

$$\hat{\mathbf{F}}_{ij} = \frac{(M_{ij} + |M_{ij}|)}{2} \begin{bmatrix} \rho_s c \\ \rho \mathbf{u} c \\ \rho h c \\ \rho e^{ve} c \end{bmatrix}_i + \frac{(M_{ij} - |M_{ij}|)}{2} \begin{bmatrix} \rho_s c \\ \rho \mathbf{u} c \\ \rho h c \\ \rho e^{ve} c \end{bmatrix}_j + P_{ij} \begin{bmatrix} 0 \\ \mathcal{I} \cdot \mathbf{n} \\ 0 \\ 0 \end{bmatrix} \tag{3.23}$$

where splitted Mach number and pressure may be expressed as:

$$M_{ij} = M_i^+ + M_j^-, \quad P_{ij} = P_i^+ + P_j^-. \tag{3.24}$$

Definition of $M_i^{\pm}$ is specified by Van Leer splitting method [38] and $P^{\pm}$ are defined as given below:

$$P^{\pm} = \begin{cases} \frac{p}{4}(M \pm 1)^2(2 \mp M) \text{ for } |M| \leq 1. \\ \frac{p}{4}(M \pm |M|)/M \text{ otherwise.} \end{cases} \tag{3.25}$$

There are also improved versions of AUSM available in SU2-NEMO which are AUSM +M [5] and AUSM^{+}up2[17]. In Maier's article[22] it is stated that, the AUSM group of schemes provides greater shock capturing while preventing the development of carbuncles, which are frequently seen in stagnation areas of blunt bodies. Since in the present study the model is a blunt body, AUSM is assessed as the right convective scheme.

CHAPTER 4

VALIDATION AND VERIFICATION STUDY OF NON-EQUILIBRIUM FLOW

Number of validation and verification studies of SU2-NEMO is limited since it is a recent developed solver of SU2. Especially to observe the validation case of surface heat flux, there is only one study found which is in Maier's article published in 2021 [22]. It was therefore decided to conduct a validation and verification study to ensure the surface heat flux distribution. Mars pathfinder experimental vehicle's model is used for the study since both experimental study and numerical study results are available in the literature and it is a clear case to validate hypersonic laminar flow solver with non-equilibrium effects. This validation and verification study has also published in 2nd International Conference on Flight Vehicles Aerothermodynamics and Re-entry Missions Engineering 2022 [4].

4.1 Model Geometry and Mesh

The model section used for non-equilibrium flow analysis is given in Figure 4.1. The dimensions are the true values of mars pathfinder experimental vehicle. Since it is an axi-symmetrical model, centerline of the geometry is defined as symmetry line to decrease the mesh size of the domain. In addition to this, only the leading front of the model is used to see surface heat flux distribution.

Final model mesh with the corresponding boundary conditions is given in Figure 4.2. Total number of mesh elements is 91312 in the form of quadratic elements. First layer thickness is defined as $10^{-}6$ m. Flow is resolved with this model and mesh conditions.

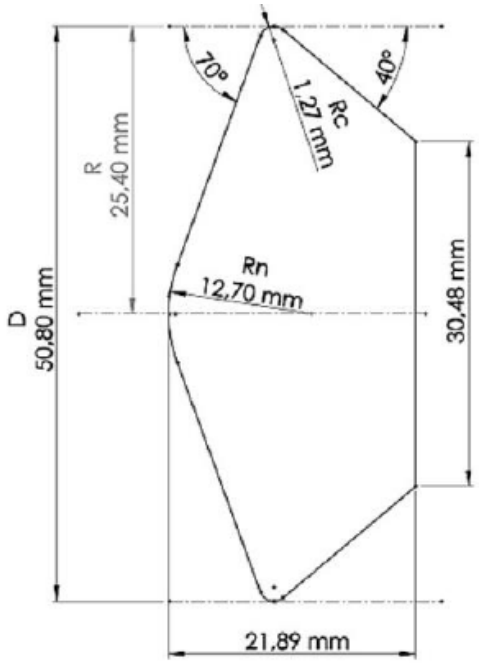

Figure 4.1: Geometric Details of the Validation Model [29]

More details about the flow domain and its mesh can be found in reference [4].

4.2 Boundary Conditions

Experiment conditions of the Mars pathfinder capsule are modeled with SU2-NEMO and two dimensional axisymmetric CFD analysis with 5 species air model ($0.77\% N_2$, $23\% O_2$) is conducted. Flow is approximated as laminar due to low density of the boundary conditions, similar to previous studies. As it is explained in previous chapter in detail, Navier-Stokes equations with non-equilibrium flow effects are discretized with finite volume method to model the flow physics. As a convective flux scheme, advective upstream splitting (AUSM) method is used since it has a good capability of shock capturing with less dissipativity [11]. Viscous fluxes are discretized at the median dual grid interfaces and Weighted Least Squares algorithm is used for gradient calculation. Thermochemical constants and reactions of 5-species air model is given in appendix. These properties are provided by importing external library, Mutation++. Experiment conditions given in Table 4.1 are applied to farfield boundary, supersonic outlet boundary condition is given to outlet boundary, wall is identified with isothermal wall boundary condition with 300 K magnitude. Lastly, symmetry

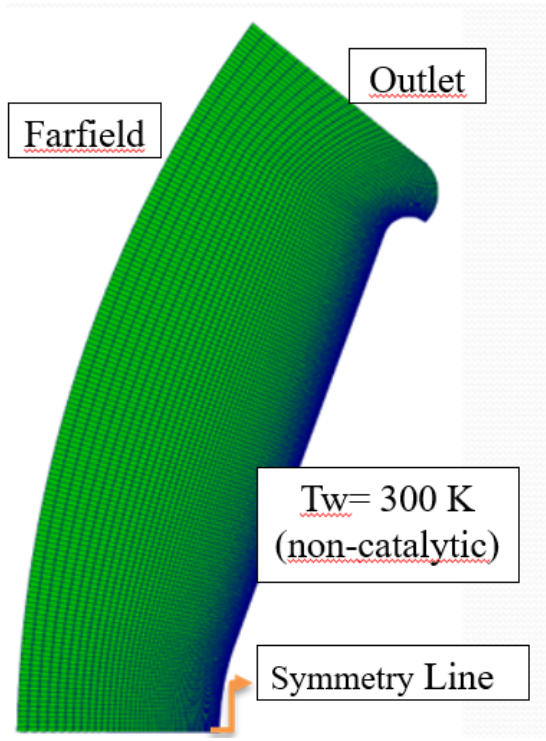

Figure 4.2: Fluid Domain and Mesh of Pathfinder Experimental Vehicle [4]

boundary condition is applied to the symmetry line.

Table 4.1: Boundary Conditions of the Mars Pathfinder Experiment

$T_\infty(K)$	$V_\infty(m/s)$	$\rho_\infty(kg/m^3)$	N_2	O_2	NO	N	O
1133	5167	5.71E-3	0.77	0.23	0	0	0

4.3 Results and Conclusion

In Figure 4.3a mach contour of the fluid domain clearly shows the strong detached bow shock wave. To validate this work, surface heat flux data is taken and compared with Hollis' experimental study [15] and Morerira's CFD analysis done with LeMANS [29], the outcome of the study can be seen in Figure 4.3b. NEMO results show a good agreement with experimental data and LeMANS' results. Starting point of the result data is the nose tip of the geometry where the heat flux is maximum as it it is also seen in the graph. Since non-catalytic isothermal wall with 300 K boundary condition is used on the surface, underprediction of surface heat flux is expected. In NEMO, partially catalytic wall boundary condition is not yet available so that non-catalytic wall with isothermal wall temperature is evaluated as a better alternative.

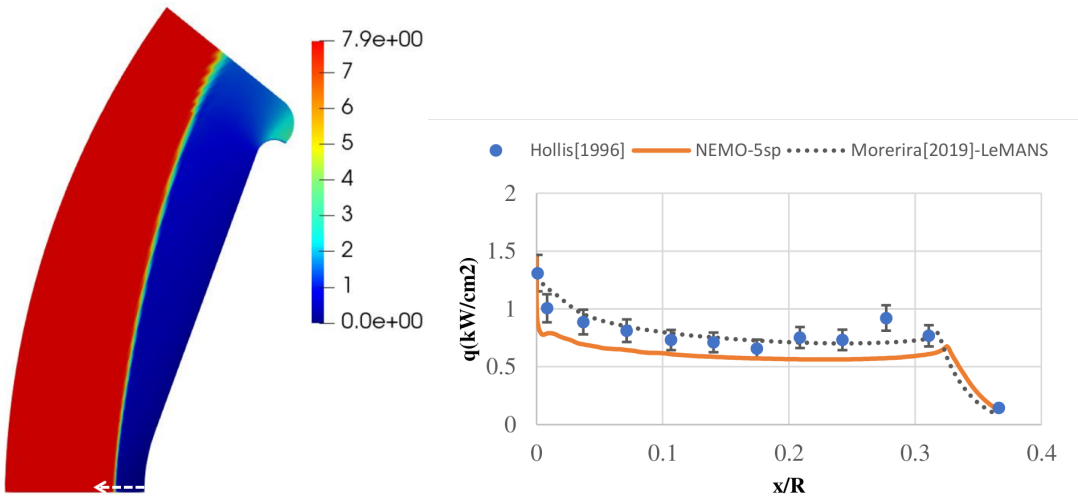

(a) (b)

Figure 4.3: Mach contour of the CFD analysis for Mars Pathfinder (a) and the heat flux distribution comparison on the surface of the blunt body (b).

Due to the fact that the existing experimental data and LeMANS CFD analysis results are taken from near nose points and throughout the symmetry line, results comparison mostly focuses on this field as it can be seen on figures. For temperature and mass fraction of the air species results the given dashed white line in Figure 4.3a is used. Temperature levels are quite high as it is expected, In Figure 4.4 results of temperature modes are given and highest translational-rotational temperature is around 12000 K orders, behind the shock it decreases to around 7000 K. This 5000 K difference is another factor that shows the strongness of the shock. The comparison of LeMANS and NEMO results presents that the both solvers calculates nearly the same temperature distribution for this current test case. In Figure 4.5 chemical species' distributions on the nose front are compared with LeMANS code results [22]. Again there is a good agreement between Moreira's results and NEMO. It can be said that the shock capturing of the two tools for current conditions are comparable.

As a result of this validation and verification study, SU2-NEMO's non-equilibrium flow modeling capability has been validated and verified once more for a hypersonic laminar flow test case. Even though, it is a recent developed solver, the result comparison with a well proven non-equilibrium flow solver LeMANS shows that it is already a competitive non-equilibrium flow modeling tool.

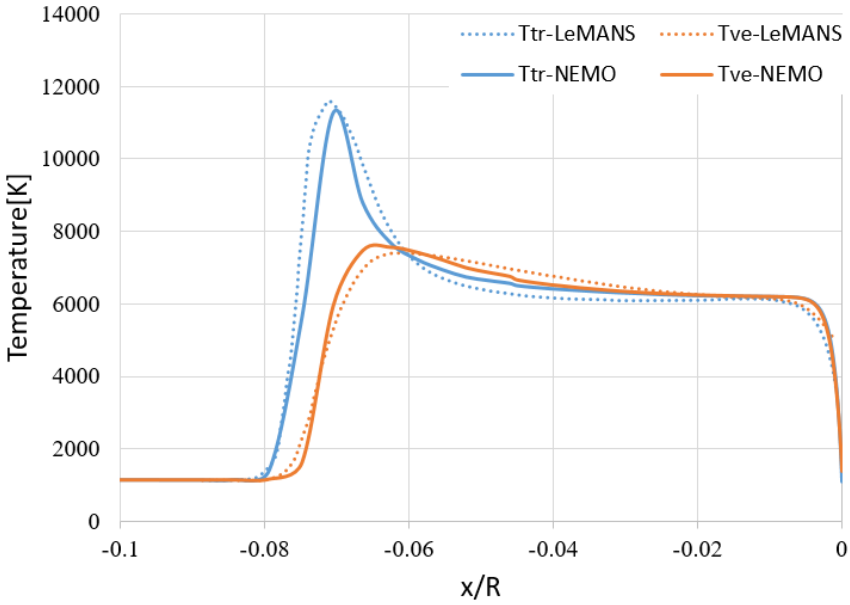

Figure 4.4: Comparison of Trans-Rotational and Vibrational-Electronic Energy Temperature Modes Results Through the Symmetry Line

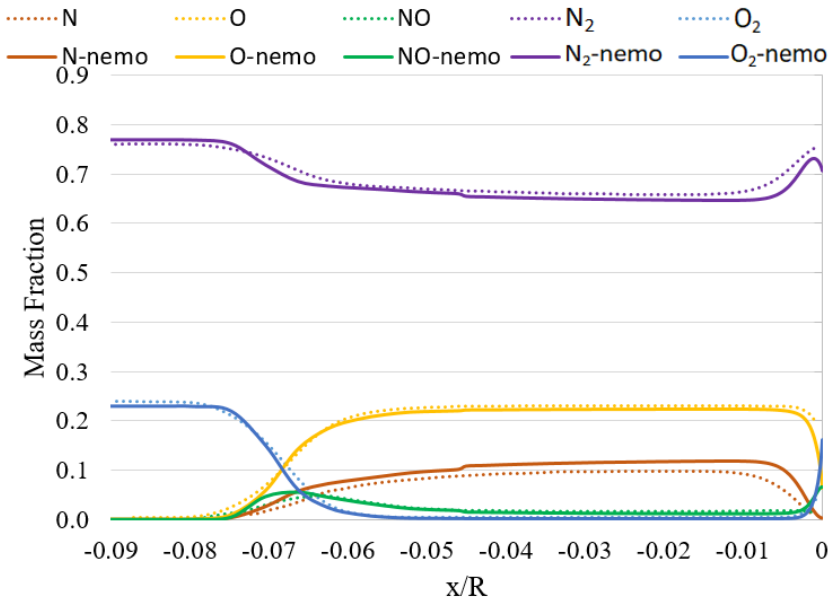

Figure 4.5: Comparison of Chemical Species' Mass Fraction Results Through the Symmetry Line

CHAPTER 5

GRAPHITE NOSE TIP LOOSELY COUPLED MODELING AND RESULTS

5.1 Problem Definition

From the literature, one experimental study of an ablation with graphite specimen subjected to an arc-jet flow [7] is chosen since its experimental conditions are close to the Mars pathfinder capsule and would be a good model to simulate hypersonic flow over blunt body. The specimen's nose radius is 19.05 mm and it has a conic body ($10°$). The test conditions which are also the boundary conditions of the non-equilibrium flow CFD analysis, given in Table 5.1. The air model is actually 5 species air model but in this particular case, oxygen molecules are entirely decomposed so that there are oxygen atoms and NO fractions in the mixture. Reactions occur in 5 species air mixture is given below:

$$\mathrm{NO} + \mathrm{M} \rightleftharpoons \mathrm{N} + \mathrm{O} + \mathrm{M}$$

$$\mathrm{O_2} + \mathrm{M} \rightleftharpoons 2\mathrm{O} + \mathrm{M}$$

$$\mathrm{N_2} + \mathrm{M} \rightleftharpoons 2\mathrm{N} + \mathrm{M}$$

$$\mathrm{N_2} + \mathrm{O} \rightleftharpoons \mathrm{N} + \mathrm{O} + \mathrm{M}$$

$$\mathrm{NO} + \mathrm{O} \rightleftharpoons \mathrm{N} + \mathrm{O_2}$$

Table 5.1: Boundary Conditions of the CFD Analysis

$T_\infty(K)$	$V_\infty(m/s)$	$\rho_\infty(kg/m^3)$	N_2	O_2	NO	N	O
1428	5354	0.03	0.6169	0	0.0046	0.1212	0.2573

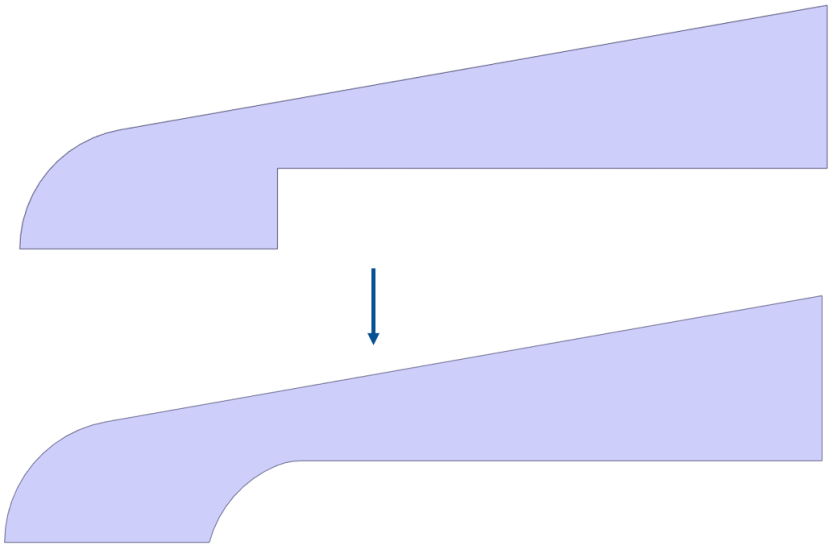

Figure 5.1: Solid Domain for Ablation Analysis

5.2 Model Geometry and Mesh

Since the geometry is a conic body with spherical nose tip, axi-symmetrical model is used for both solid domain (material response/ablation analysis) and fluid domain (CFD analysis) parts. For the solid domain a small modification by adding a radius to the sharp edge of the specimen is done to generate better mesh. The geometry change of the solid domain is shown in Figure 5.1 and fluid domain is with corresponding geometry dimensions is given in Figure 5.2 A mesh study with 3 different structured mesh size is conducted for fluid domain. First mesh is the coarse mesh with size 28×63, second one is the medium mesh with size 75×126 and the last one is the fine mesh with size 114×189. The result of the study is given in Figure 5.3 as surface heat flux distribution. The average difference between coarse and medium meshes is 28% and maximum difference is calculated as 37% near stagnation point. Due to this large variation, fine mesh is examined. The average heat flux difference between fine and medium meshes is calculated as 3.4% and the maximum difference is around 10% which is again around stagnation point. As a result, medium mesh with 75×126 grid elements is selected as the final mesh instead of using fine mesh with 2.2 times larger computational domain. Mesh domain can be seen in Figure 5.4a, 300

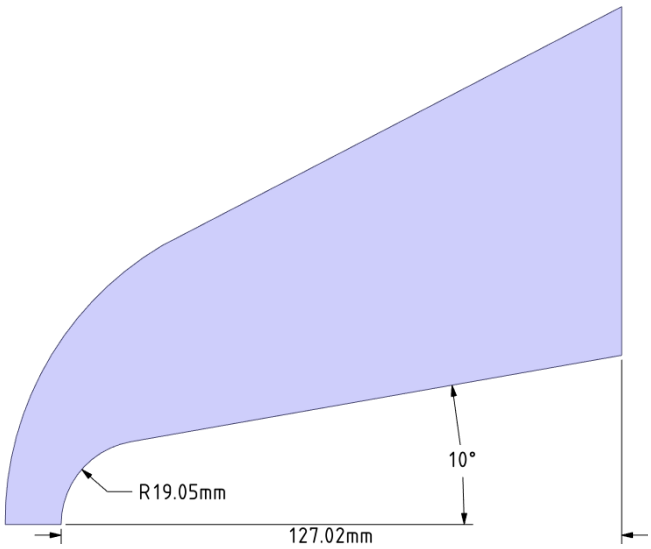

Figure 5.2: Fluid Domain for CFD Analysis

K isothermal boundary condition is defined to walls of the blunt body and supersonic outlet boundary condition is given to right side boundary of the domain. For the solid domain a fine mesh by using the test cases mesh sizes is generated and resulting mesh consisting of 18351 elements is given in Figure 5.4b.

5.3 Flow Domain Analyis and Results

Hypersonic air flow is considered laminar similar to previous studies. The boundary conditions given in Table 5.1 is applied to the farfield boundary. First, it is decided to neglect the viscous effects to provide a more steady initial condition for Navier-Stokes analysis. Therefore, 40000 iterations are solved by euler equations by defining the wall boundary condition as inviscid wall at the first part of analysis. Then, Navier Stokes equations with thermodynamic non-equilibrium effects are solved for the blunt body fluid domain for 70000 iterations before obtaining convergence. Mach contour clearly shows the detached bow shock wave with high intensity of hypersonic flow in Figure 5.5. In the same figure, heat flux and pressure distribution on the blunt body surface is also given which is used as the input of the ablation solver PATO.

Temperature results for translational-rotational temperature mode and vibrational-electronic energy mode are given in and Figure 5.6. Recovery temperature near stag-

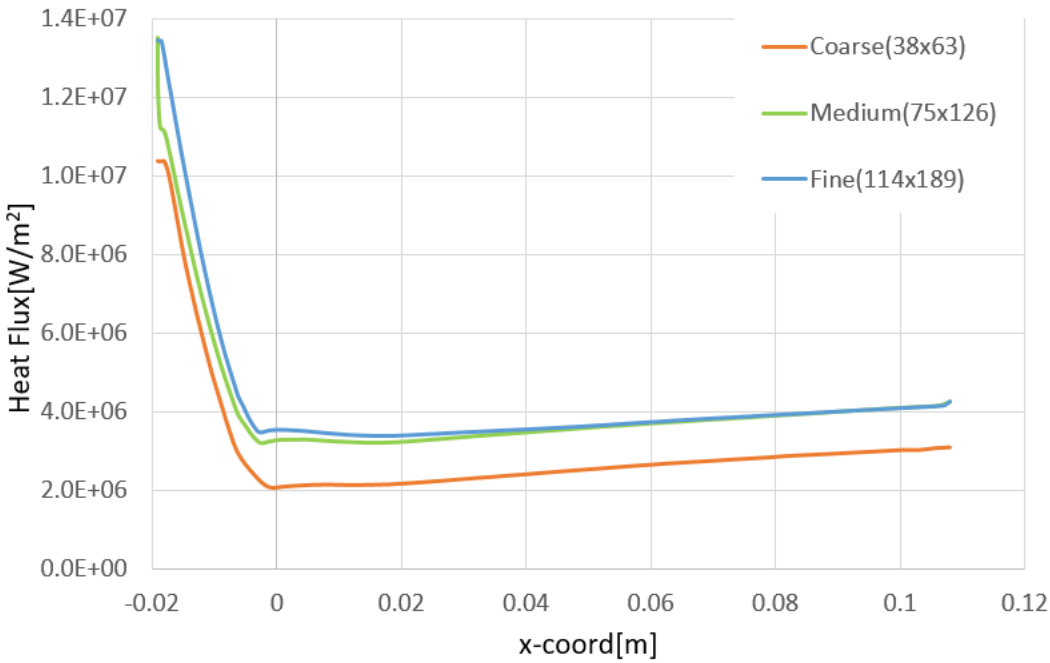

Figure 5.3: Solid Domain for Ablation Analysis

nation region is found as 12770 K. This value is used for recovery enthalpy calculation. In Figure 5.7a N species distribution over the surface in mass fraction unit are shown, beside it change of all species mass fraction through the black line shown in the stagnation region of Figure 5.7a is given. These contours are consistent with the boundary conditions.

5.4 Coupling Methodology and Ablation Analysis

Surface heat flux distribution is extracted from the CFD result with the Python script "$pato\_bc\_maker.py$" which is given in appendix A and used as convective heat flux boundary condition of solid domain analysis. In the surface energy balance equation of PATO, convective heat flux is defined as function of boundary layer edge properties ([$q_{\text{conv}} = \rho_e u_e C'_H (h_e - h_w)$ so that it is not a proper way to use convective heat flux value directly which means ignoring the surface blowing effect (B'). By using local velocity, local density, recovery temperature and the wall temperature values which are basically calculated by isentropic relations, Stanton number (C_H) is calculated. At the end $\rho_e u_e C_H$ multiplication and the edge enthalpy ($h_e = c_p T_r$) are defined as the boundary conditions of PATO. For the inner boundaries of solid domain, adiabatic

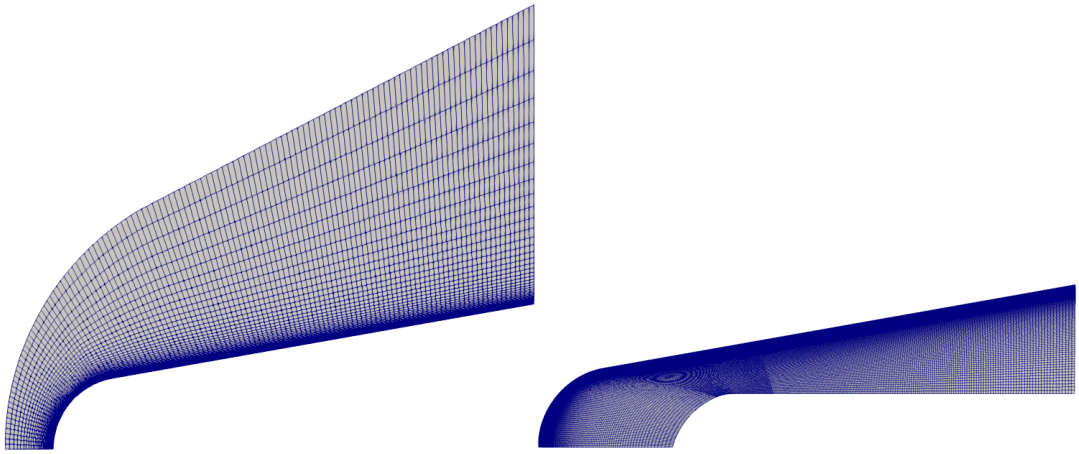

(a) (b)

Figure 5.4: Fluid mesh domain of the CFD model(a), solid mesh domain of the ablation model(b)

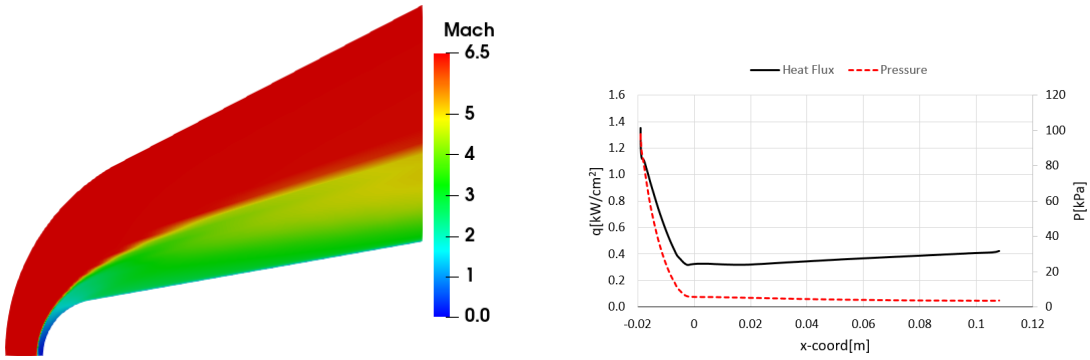

(a) (b)

Figure 5.5: Mach contour of the CFD analysis (a), the heat flux and pressure distribution on the surface of the blunt body (b).

wall boundary condition is used because it is not expected to see temperature gradient in inner regions of the solid domain. Again, axisymmetrical model is used for the analysis and Type 3 ablation equations of PATO are solved to model the physics of the problem. The material of the test specimen is graphite as it is stated before, thermochemical properties of graphite is found on the literature and added to Mutation++ library. Temperature depended specific heat (c_p), thermal conductivity(k) and enthalpy are shown in Figure 5.8. These properties are taken from NIST TRC Thermodynamic Tables [2]. Since there is no pyrolysis reactions occur in graphite the sublimation reaction is the main reason of heat absorption which starts around 3500 K (sublimation reaction of graphite: $3C(s) \rightarrow C_3(g)$).

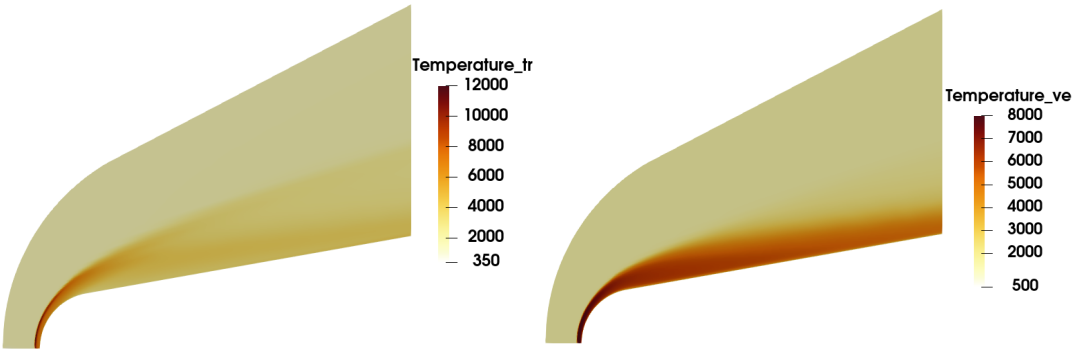

(a) (b)

Figure 5.6: Translational-Rotational temperature mode contour (a) and Vibrational-Electronic Energy Contour the (b).

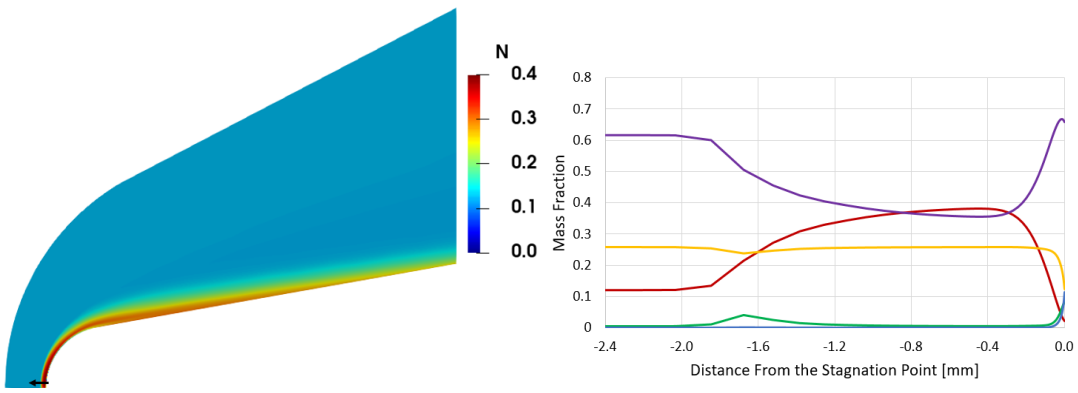

(a) (b)

Figure 5.7: N species distribution contour due to dissociation reaction near wall (a) and mass fraction of all species through the line (b).

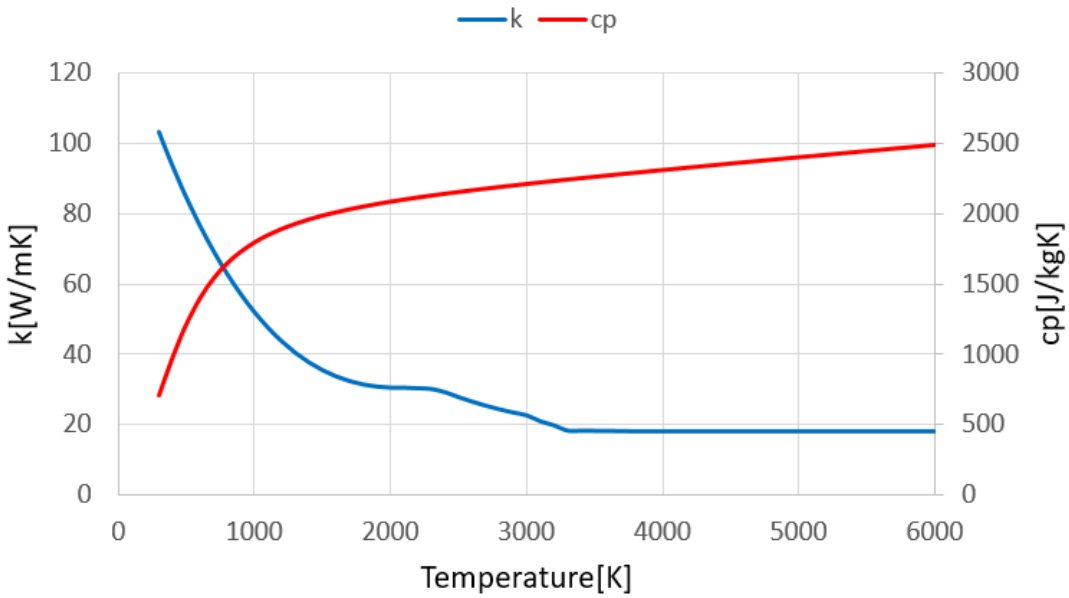

(a)

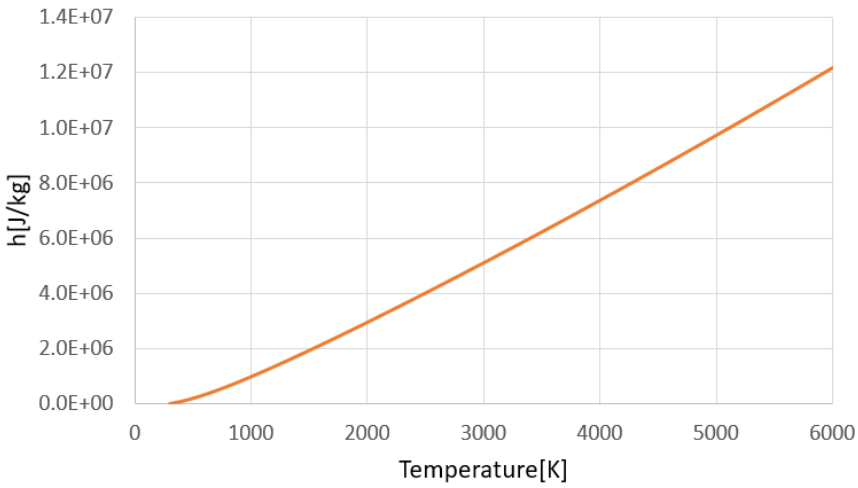

(b)

Figure 5.8: Thermal conductivity and specific heat of the graphite (a), the heat flux and pressure distribution on the surface of the blunt body (b).

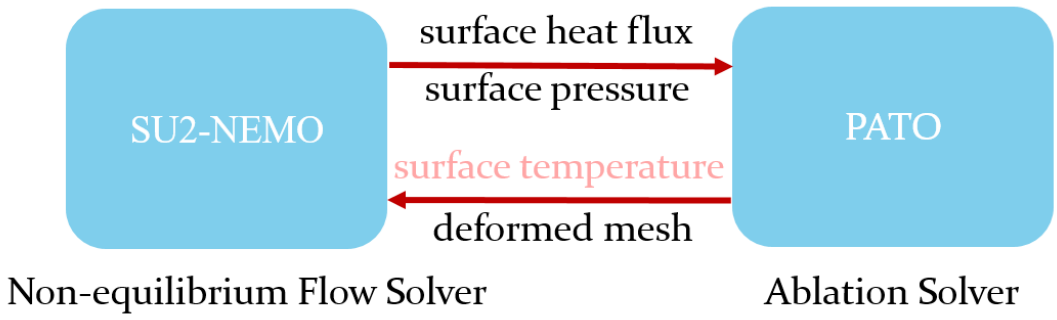

Figure 5.9: Coupling Methodology of the Analysis

Total duration of the analysis is thirty seconds due to related experiment and in total six CFD analysis is conducted which means each PATO analysis is transient and five seconds long. In each coupling iteration, deformed surface mesh and wall temperature distribution from PATO are planned to be taken as output by using python script and used as updated isothermal wall boundary condition but due to a mpi4py library problem in Python 3, the script for mapping temperature ($T\_mapper.py$) could not be executed. Therefore, coupling is accomplished by using surface recession data without surface temperature distribution. This general coupling structure can be seen in Figure 5.9.

By exporting the deformed surface mesh, open source mesh and design software Salome is used to make necessary geometry operations. The main problem was that PATO is an openFoam based solver and openFOAM uses 3D models for axisymmetrical analysis. From that 3D model, upper surface of the solid domain is extracted and it is converted to 1D line with the help of self developed python script (in appendix B: $surf\_to\_edge.py$). Farfield line of the first domain is imported to Salome in each coupling iteration. Another Python script $su2\_mesher.py$ given in appendix C uses farfield and deformed surface lines' corner points to create a face from these 2 lines. After creating the surface it automatically generates the new mesh of the new fluid domain for next CFD analysis. Detailed schematic with the names of the python scripts used in each coupling step is shown in Figure 5.10 with related illustrations.

The solution contours, time dependent temperature and surface recession graphs are shared and the comparison study with previous studies and experimental data is conducted in next section.

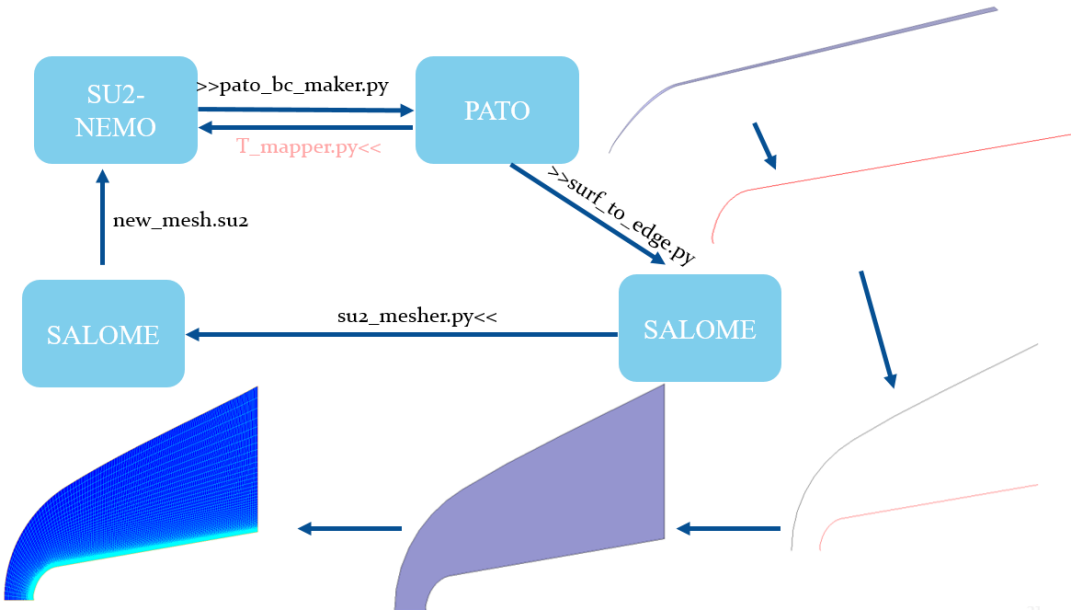

Figure 5.10: Detailed Schematic of the Coupling Procedure

5.4.1 Results

Due to higher flux on the nose tip, bluntness of the geometry has increased at the end of the ablation analysis as it is expected. Temperature contour of the model at the last time step with the undeformed geometry marks is given in Figure 5.11. As it is seen the maximum temperature is about 3500 K and recession of nose tip much higher than the conic section of the specimen as it is expected. Recession of two points (stagnation point and point on $45°$) are used to validate analysis result. In Figure 5.12, the agreement between experimental data [7] is clearly seen. The reason of the difference can be the thermo-chemical properties of graphite since it is not given in the experimental study. On the other hand, non-catalytic wall boundary condition may have caused to underestimation of the surface heat flux which can explain the lower recession calculated in ablation analysis.

Temperature distribution of the two dimensional PATO analysis result at last time step is shown in Figure 5.13. The comparison of the current study's result with Bianchi's [2], Onay's [32] computations and Chen and Milos' experimental study is carried out. For the conic part of the geometry PATO has a better agreement with experimental results but near stagnation area temperature drops earlier with respect to computation results and experimental data. This difference may be due to the coupling interval.

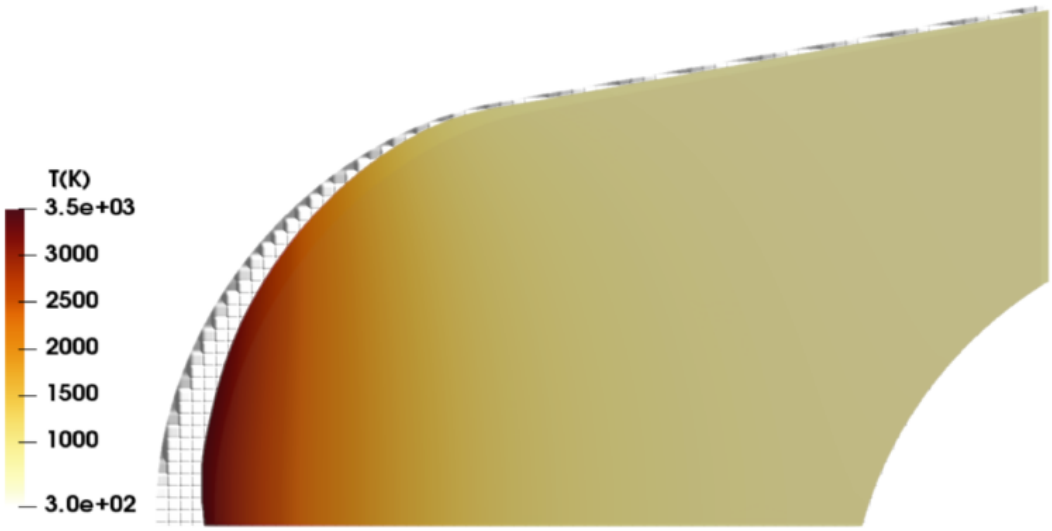

Figure 5.11: Temperature distribution of graphite nose tip at the last time step of the ablation analysis

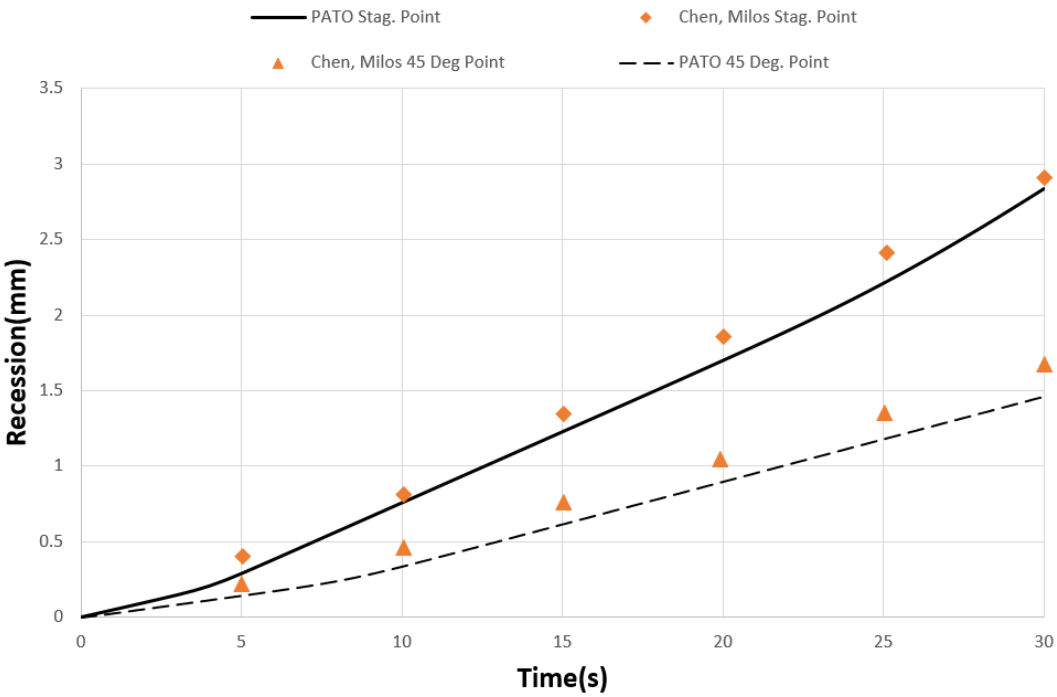

Figure 5.12: Recession of Stagnation Point and 45° Point

Since a loosely coupled analysis is conducted here, heat flux distribution used as input of the PATO analysis was not the most accurate boundary condition for each time step. It is updated in every 5 seconds. Heat flux distributions of different coupling steps (at first, $t = 10s$ and last time steps) are given in Figure 5.14 which also supports this claim since there is a clear change on the pattern of the heat flux values due to the change of surface bluntness of the geometry.

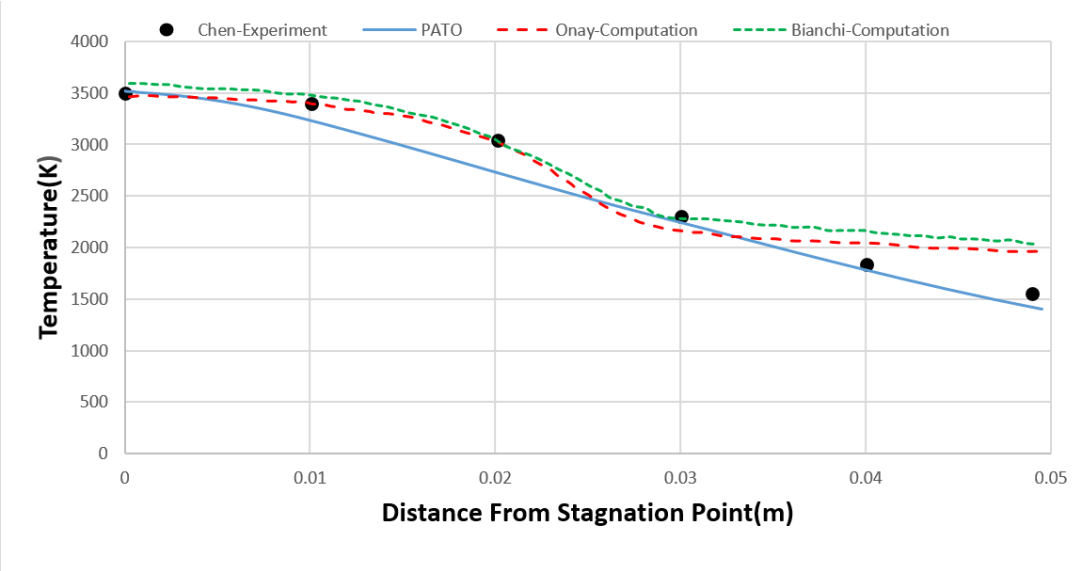

Figure 5.13: Temperature Distribution Validation

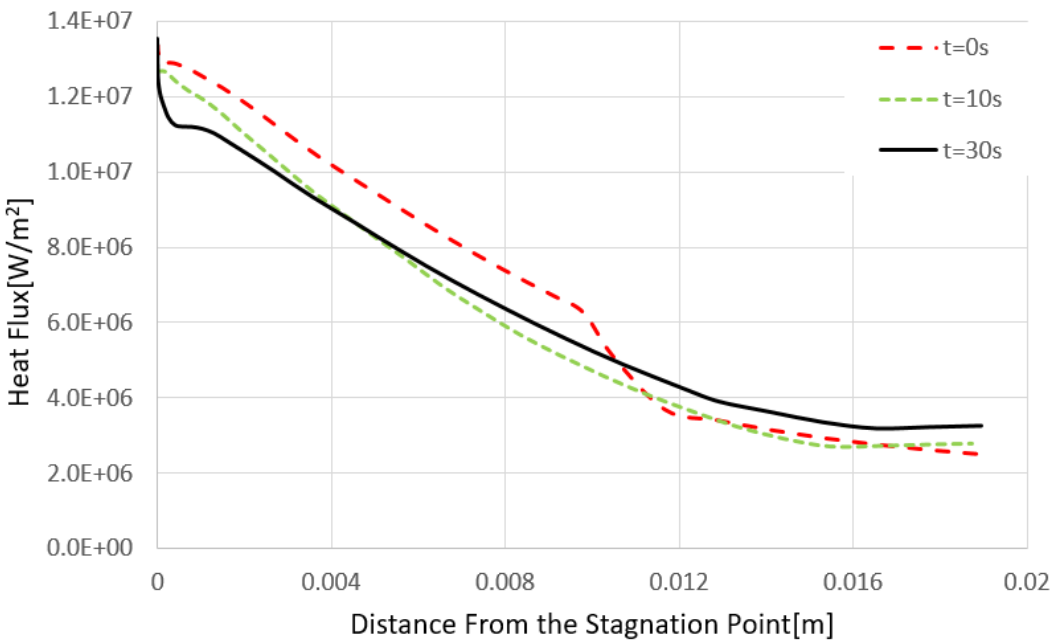

Figure 5.14: Surface Recession

5.5 Conclusion

For an hypersonic aerospace vehicle under high enthalpy flow, shape change due to surface recession has an impact on heat flux distributions even though the peak heat flux value remain nearly unchanged and the flux orders are similar. Therefore, when there is a need for more accurate computation of thermal boundary conditions, ablation effects can be considered but as it is seen in Figure 5.14 the order of the heat flux does not change with shape change (only the mapped fluxes have different patterns). On the other hand, from aero-thermal design point of view thermal boundary conditions are not the only concerns during an aerospace vehicle design, change of aerodynamic coefficients and center of gravity also have a significant role which are not the concerns of the current study.

All in all, by using two open source softwares (PATO and SU2), loosely coupled ablation-nonequilibrium flow simulation tool is builded up and validated as an output of this thesis. It is used to show the effect of surface recession on heat flux distribution.

5.6 Future Work

It is planning to add the temperature coupling to this study to finalize it. A separate study regarding the coupling frequency and its effect on heat flux distribution is also considered as future work of this study. Lastly, a fully coupled simulation of PATO and SU2 NEMO solvers is intended to be accomplished as a future work.

REFERENCES

[1] A. J. Amar et al., Modeling of one-dimensional ablation with porous flow using finite control volume procedure, 2006.

[2] D. Bianchi, Modeling of ablation phenomena in space applications, 2007.

[3] V. Casseau, T. J. Scanlon, and R. E. Brown, Development of a two-temperature open-source cfd model for hypersonic reacting flows, in *20th AIAA International Space Planes and Hypersonic Systems and Technologies Conference*, p. 3637, 2015.

[4] M. Celik, O. Uğur, and S. Eyi, Numerical modeling of hypersonic air and carbon dioxide flows in thermochemical non-equilibrium with su2-nemo solver, International Conference on Flight Vehicles, Aerothermodynamics and Re-entry Missions Engineering, 2022.

[5] S. Chen, F. Cai, H. Xue, N. Wang, and C. Yan, An improved ausm-family scheme with robustness and accuracy for all mach number flows, Applied Mathematical Modelling, 77, 2020.

[6] Y. K. Chen and F. S. Milos, Ablation and thermal response program for spacecraft heatshield analysis, Journal of Spacecraft and Rockets, 36, 1999.

[7] Y. K. Chen, F. S. Milos, D. C. Reda, and D. A. Stewart, Graphite ablation and thermal response simulation under arc-jet flow conditions, 36th AIAA Thermophysics Conference, 2002.

[8] D. M. Curry, An analysis of charring ablation thermal protection system, 1965.

[9] T. Economon, F. Palacios, S. Copeland, T. Lukaczyk, and J. Alonso, Su2: An open-source suite for multiphysics simulation and design, AIAA J., 54, 2016.

[10] H. J. Ene and E. Sanchez-Palencia, On thermal equation for flow in porous media, International Journal of Engineering Science, 20, 1982.

[11] C. Garbacz, W. T. Maier, J. B. Scoggins, T. D. Economon, T. Magin, J. J. Alonso, and M. Fossati, Shock interactions in inviscid air and co2-n2 flows in thermochemical non-equilibrium, Shock Waves, 31, 2021.

[12] P. Gnoffo and R. McCandless, Three-dimensional aotv flowfields in chemical nonequilibrium, in *24th Aerospace Sciences Meeting*, p. 230, 1986.

[13] P. A. Gnoffo, Review of a code development and calibration program in support of the aeroassist flight experiment, 1989.

[14] J. M. Grimwood, B. C. Hacker, and P. J. Vorzimmer, *Project Gemini technology and operations - A chronology, NASA*, Scientific and Technical Information Division, National Aeronautics and Space Administration, 1969.

[15] B. R. Hollis and J. N. Perkins, High enthalpy and perfect gas heating measurements on a blunt cone, AIAA Journal of Spacecraft and Rockets, 33, 1996.

[16] J. KEENAN and G. CANDLER, Simulation of ablation in earth atmospheric entry, in *28th Thermophysics Conference*, p. 2789, 1993.

[17] K. Kitamura and E. Shima, Towards shock-stable and accurate hypersonic heating computations: A new pressure flux for ausmfamily schemes, Journal of Computational Physics, 245, 2013.

[18] J. Lachaud, I. Cozmuta, and N. N. Mansour, Multiscale approach to ablation modeling of phenolic impregnated carbon ablators, Journal of Spacecraft and Rockets, 47, 2010.

[19] J. Lachaud, T. E. Magin, I. Cozmuta, and N. N. Mansour, A short review of ablative-material response models and simulation tools, 7th aerothermodynamics symposium, No. ARC-E-DAA-TN3517, 2011.

[20] J. Lachaud and N. N. Mansour, Porous-material analysis toolbox based on openfoam and applications, Journal of Thermophysics and Heat Transfer, 28, 2014.

[21] A. Lani, N. Villedie, K. Bensassi, L. Koloszar, M. Vymazal, S. M. Yalim, and M. Panesi, Coolfluid: an open computational platform for multi-physics simulation and research, in *21st AIAA Computational Fluid Dynamics Conference*, p. 2589, 2013.

[22] W. T. Maier, J. T. Needels, C. Garbacz, F. Morgado, J. J. Alonso, and F. M., Su2-nemo: An open-source framework for high-mach nonequilibrium multi-species flows, Aerospace, 8(7), 2021.

[23] J. Marschall and F. S. Milos, Gas permeability of rigid fibrous refractory insulations, Journal of Thermophysics and Heat Transfer, 12, 1998.

[24] A. Martin and I. Boyd, Implicit implementation of material response and moving meshes for hypersonic re-entry ablation, in *47th AIAA Aerospace Sciences Meeting including The New Horizons Forum and Aerospace Exposition*, p. 670, 2009.

[25] A. Martin and I. D. Boyd, Strongly coupled computation of material response and nonequilibrium flow for hypersonic ablation, Journal of Spacecraft and Rockets, 52(1), pp. 89–104, 2015.

[26] A. Mazzarachio, One-dimensional thermal analysis model for charring ablative materials, J Aerospace Technology Management, 10, 2018.

[27] S. Meng, Y. Zhou, W. Xie, F. Yi, and S. Du, Multiphysics coupled fluid/thermal/ablation simulation of carbon/carbon composites, Journal of Spacecraft and Rockets, 53(5), pp. 930–935, 2016.

[28] R. Millikan and D. White, Systematics of vibrational relaxation, J. Chem. Phys., 39, 1963.

[29] F. C. Moreira, W. Wolf, and J. L. F. Azevedo, Investigation of thermodynamic non-equilibrium in hypersonic flows over the mars pathfinder capsule, AIAA Scitech 2021 Forum, 2021.

[30] I. Nompelis, T. Drayna, and G. Candler, Development of a hybrid unstructured implicit solver for the simulation of reacting flows over complex geometries, in *34th AIAA Fluid Dynamics Conference and Exhibit*, p. 2227, 2004.

[31] A. D. Omidy, F. Panerai, A. Martin, J. R. Lachaud, I. Cozmuta, and N. N. Mansour, Code-to-code comparison, and material response modeling of stardust and msl using pato and fiat, NASA/CR–2015–218960, 2015.

[32] O. K. Onay, Ablation modeling for high speed internal and external flows, 2020.

[33] C. Park, *Nonequilibrium Hypersonic Aerothermodynamics*, Wiley: New York, NY, USA, 1990.

[34] N. Puiroux, M. . Prat, and M. Quintard, Non-equilibrium theories for macroscale heat transfer: Ablative composite layer system, International Journal of Thermal Sciences, 43, 2004.

[35] T. Scoggins, J.B.and Magin, Development of mutation++: Multicomponent thermodynamic and transport properties for ionized plasmas written in c++, 11th AIAA/ASME joint thermophysics and heat transfer conference, 2014.

[36] T. Van Eekelen and J. Lachaud, Radiation heat-transfer model for the ablation zone of low-density carbon-resin composites, 10th AIAA/ASME Joint Thermophysics and Heat Transfer Conference, 2010.

[37] T. Van Eekelen and J. Lachaud, Numerical validation of an effective radiation heat transfer model for fiber preforms, 1Journal of Spacecraft and Rockets, 48, 2011.

[38] B. Van Leer, Flux-vector splitting for the euler equations, In Proceedings of the Eighth International Conference on Numerical Methods in Fluid Dynamics, Aachen, Germany, 170, 1982.

[39] J. D. Watts, Flight experience with shock impingement and interference heating on the x-15-2 research airplane, NASA TM X-1669, 1968.

[40] M. J. Wright, G. V. Candler, and D. Bose, Data-parallel line relaxation method for the navier-stokes equations, AIAA journal, 36(9), pp. 1603–1609, 1998.

APPENDIX A

PATO BOUNDARY CONDITION MAKER

Here the python script to prepare the boundary condition for PATO ablation analysis is presented. It uses the surface pressure and heat flux output of the CFD analysis which is obtained by a basic Paraview script and changes the data to a suitable form for flux factor mapping.

```
# -*- coding: utf-8 -*-
"""
Created on Thu Nov  3 04:31:14 2022

@author: Mutlu Çelik
"""
import numpy as np

data = np.genfromtxt('surf_p-q.csv', delimiter=',')
s_data=data[data[:, 4].argsort()]
l=s_data[len(s_data)-2, 4]+0.00005
y=s_data[:,4]
d=y-l #distance
d=d[0:125]
qmax=data[1:,1].max()
pmax=data[1:,0].max()
ii=np.where(s_data[1:,1]==qmax)
j=ii[0]+1
q_map=s_data[:125,1]/qmax
if qmax>1:
    q_map[0:j[0]]=1.0

kk=np.where(s_data[1:,0]==pmax)
jj=kk[0]+1
p_map=s_data[:125,0]/pmax
if pmax>1:
    p_map[0:jj[0]]=1.0

f_map=np.dstack((d, q_map, p_map))
np.savetxt('fluxFactorMap_', f_map, delimiter='\t')
```

Listing A.1: The *pato_bc_maker.py* script that creates the flux factor mapping for ablation analysis.

APPENDIX B

DEFORMED EDGE MAKER

In this appendix part the python script for SALOME design software is given. It basically does some cutting and compound operations to have the final edge line. The $surf\_to\_edge.py$ script that takes the 3D surface as input and gives the edge line on xy plane as the output:

```python
#!/usr/bin/env python
###
### This file is generated automatically by SALOME v9.8.0 with dump python functionality
###
import sys
import salome

salome.salome_init()
import salome_notebook
notebook = salome_notebook.NoteBook()
sys.path.insert(0, r'/home/mutlu/Desktop/pato_deneme/blunt_cone/salome_script_case')
###
### GEOM component
###
import GEOM
from salome.geom import geomBuilder
import math
import SALOMEDS

geompy = geomBuilder.New()

O = geompy.MakeVertex(0, 0, 0)
OX = geompy.MakeVectorDXDYDZ(1, 0, 0)
OY = geompy.MakeVectorDXDYDZ(0, 1, 0)
OZ = geompy.MakeVectorDXDYDZ(0, 0, 1)
Kapal__e_0_ = geompy.ImportIGES("../farfield.igs")
deformed_1_stl_1 = geompy.ImportSTL("../deformed_1.stl" )
Kapal__e_0__1 = geompy.ImportIGES("../farfield.igs")
Vertex_1 = geompy.MakeVertex(0.107975, 1e-05, 0)
Kapal__e_0__vertex_3 = geompy.GetSubShape(Kapal__e_0__1, [3])
Line_1 = geompy.MakeLineTwoPnt(Vertex_1, Kapal__e_0__vertex_3)
Line_1_vertex_2 = geompy.GetSubShape(Line_1, [2])
Kapal__e_0__vertex_2 = geompy.GetSubShape(Kapal__e_0__1, [2])
Line_2 = geompy.MakeLineTwoPnt(Line_1_vertex_2, Kapal__e_0__vertex_2)
Face_1 = geompy.MakeFaceWires([Kapal__e_0_, Line_1, Line_2], 1)
Cut_1 = geompy.MakeCutList(Face_1, [deformed_1_stl_1], True)
[Face_2,ProcessShape_1] = geompy.ExtractShapes(Cut_1, geompy.ShapeType["FACE"], True)
ProcessShape_1 = geompy.ProcessShape(Face_2, ["FixShape", "FixFaceSize", "DropSmallEdges", "SameParameter"],..
 "FixShape.Tolerance3d", "FixShape.MaxTolerance3d", "FixFaceSize.Tolerance", "DropSmallEdges.Tolerance3d",..
 "SameParameter.Tolerance3d"], ["1e-07", "1", "0.05", "0.05", "1e-07"])
[Edge_1,Edge_2,Edge_3] = geompy.ExtractShapes(ProcessShape_1, geompy.ShapeType["EDGE"], True)
geompy.ExportSTEP(Edge_2, "/home/mutlu/Desktop/pato_deneme/blunt_cone/salome_script_case/deformed_wall.step", GEOM.LU_METER )
geompy.addToStudy( O, 'O' )
geompy.addToStudy( OX, 'OX' )
geompy.addToStudy( OY, 'OY' )
geompy.addToStudy( OZ, 'OZ' )
geompy.addToStudy( Kapal__e_0_, 'Kapal_ e(0)' )
geompy.addToStudy( deformed_1_stl_1, 'deformed_1.stl_1' )
geompy.addToStudy( Kapal__e_0__1, 'Kapal_ e(0)' )
geompy.addToStudy( Vertex_1, 'Vertex_1' )
geompy.addToStudyInFather( Kapal__e_0__1, Kapal__e_0__vertex_3, 'Kapal_ e(0):vertex_3' )
geompy.addToStudy( Line_1, 'Line_1' )
geompy.addToStudyInFather( Line_1, Line_1_vertex_2, 'Line_1:vertex_2' )
geompy.addToStudyInFather( Kapal__e_0__1, Kapal__e_0__vertex_2, 'Kapal_ e(0):vertex_2' )
geompy.addToStudy( Line_2, 'Line_2' )
geompy.addToStudy( Face_1, 'Face_1' )
geompy.addToStudy( Cut_1, 'Cut_1' )
geompy.addToStudyInFather( Cut_1, Face_2, 'Face_2' )
geompy.addToStudy( ProcessShape_1, 'ProcessShape_1' )
geompy.addToStudyInFather( ProcessShape_1, Edge_1, 'Edge_1' )
geompy.addToStudyInFather( ProcessShape_1, Edge_2, 'Edge_2' )
geompy.addToStudyInFather( ProcessShape_1, Edge_3, 'Edge_3' )
exit()

if salome.sg.hasDesktop():
  salome.sg.updateObjBrowser()
```

Figure B.1: $surf\_to\_edge.py$ script

APPENDIX C

SU2 MESHER

The Python script of SALOME given in this appendix generates the 2D flow domain mesh by using the deformed wall edge of solid domain and the farfield edge of flow domain. Firstly, 2D flow domain plane is generated by using the corner points and edges themselves than that face is used to have flow domain mesh. The script is given below:

```python
#!/usr/bin/env python

###
### This file is generated automatically by SALOME v9.8.0 with dump python functionality
###

import sys
import salome

salome.salome_init()
import salome_notebook
notebook = salome_notebook.NoteBook()
sys.path.insert(0, r'/home/mutlu/SALOME-9.8.0-native-UB20.04-SRC')

###
### GEOM component
###

import GEOM
from salome.geom import geomBuilder
import math
import SALOMEDS


geompy = geomBuilder.New()

O = geompy.MakeVertex(0, 0, 0)
OX = geompy.MakeVectorDXDYDZ(1, 0, 0)
OY = geompy.MakeVectorDXDYDZ(0, 1, 0)
OZ = geompy.MakeVectorDXDYDZ(0, 0, 1)
Kapal__e_0_ = geompy.ImportIGES("../farfield.igs")
deformed_wall_step_1 = geompy.ImportSTEP("../deformed_wall.step", False, True)
deformed_wall_step_1_vertex_3 = geompy.GetSubShape(deformed_wall_step_1, [3])
Kapal__e_0__vertex_3 = geompy.GetSubShape(Kapal__e_0_, [3])
Line_1 = geompy.MakeLineTwoPnt(deformed_wall_step_1_vertex_3, Kapal__e_0__vertex_3)
deformed_wall_step_1_vertex_4 = geompy.GetSubShape(deformed_wall_step_1, [4])
Kapal__e_0__vertex_2 = geompy.GetSubShape(Kapal__e_0_, [2])
Line_2 = geompy.MakeLineTwoPnt(deformed_wall_step_1_vertex_4, Kapal__e_0__vertex_2)
Face_1 = geompy.MakeFaceWires([Kapal__e_0_, deformed_wall_step_1, Line_1, Line_2], 1)
sym = geompy.CreateGroup(Face_1, geompy.ShapeType["EDGE"])
geompy.UnionIDs(sym, [10])
wall = geompy.CreateGroup(Face_1, geompy.ShapeType["EDGE"])
geompy.UnionIDs(wall, [8])
outlet = geompy.CreateGroup(Face_1, geompy.ShapeType["EDGE"])
geompy.UnionIDs(outlet, [6])
farfield = geompy.CreateGroup(Face_1, geompy.ShapeType["EDGE"])
geompy.UnionIDs(farfield, [3])
[sym, wall, outlet, farfield] = geompy.GetExistingSubObjects(Face_1, False)
geompy.addToStudy( O, 'O' )
geompy.addToStudy( OX, 'OX' )
geompy.addToStudy( OY, 'OY' )
geompy.addToStudy( OZ, 'OZ' )
geompy.addToStudy( Kapal__e_0_, 'Kapal_ e(0)' )
geompy.addToStudy( deformed_wall_step_1, 'deformed_wall.step_1' )
geompy.addToStudyInFather( deformed_wall_step_1, deformed_wall_step_1_vertex_3, 'deformed_wall.step_1:vertex_3' )
geompy.addToStudyInFather( Kapal__e_0_, Kapal__e_0__vertex_3, 'Kapal_ e(0):vertex_3' )
geompy.addToStudy( Line_1, 'Line_1' )
geompy.addToStudyInFather( deformed_wall_step_1, deformed_wall_step_1_vertex_4, 'deformed_wall.step_1:vertex_4' )
geompy.addToStudyInFather( Kapal__e_0_, Kapal__e_0__vertex_2, 'Kapal_ e(0):vertex_2' )
geompy.addToStudy( Line_2, 'Line_2' )
geompy.addToStudy( Face_1, 'Face_1' )
geompy.addToStudyInFather( Face_1, sym, 'sym' )
geompy.addToStudyInFather( Face_1, wall, 'wall' )
geompy.addToStudyInFather( Face_1, outlet, 'outlet' )
geompy.addToStudyInFather( Face_1, farfield, 'farfield' )

###
### SMESH component
###

import  SMESH, SALOMEDS
from salome.smesh import smeshBuilder

smesh = smeshBuilder.New()
#smesh.SetEnablePublish( False )
# Set to False to avoid publish in study if not needed or in some particular situations:
# multiples meshes built in parallel, complex and numerous mesh edition (performance)

Mesh_1 = smesh.Mesh(Face_1)
Quadrangle_2D = Mesh_1.Quadrangle(algo=smeshBuilder.QUADRANGLE)
Quadrangle_Parameters_1 = Quadrangle_2D.QuadrangleParameters(smeshBuilder.QUAD_QUADRANGLE_PREF,-1,[],[])
sym_1 = Mesh_1.GroupOnGeom(sym,'sym',SMESH.EDGE)
wall_1 = Mesh_1.GroupOnGeom(wall,'wall',SMESH.EDGE)
outlet_1 = Mesh_1.GroupOnGeom(outlet,'outlet',SMESH.EDGE)
farfield_1 = Mesh_1.GroupOnGeom(farfield,'farfield',SMESH.EDGE)
Regular_1D = Mesh_1.Segment(geom=sym)
```

Figure C.1: First part of *su2_mesher.py* script

```
86  Number_of_Segments_1 = Regular_1D.NumberOfSegments(100,500,[])
87  Regular_1D_1 = Mesh_1.Segment(geom=outlet)
88  Number_of_Segments_2 = Regular_1D_1.NumberOfSegments(100,3100,[])
89  Regular_1D_2 = Mesh_1.Segment(geom=wall)
90  Number_of_Segments_3 = Regular_1D_2.NumberOfSegments(126,1,[])
91  Regular_1D_3 = Mesh_1.Segment(geom=farfield)
92  Number_of_Segments_4 = Regular_1D_3.NumberOfSegments(126,0.3,[])
93  isDone = Mesh_1.Compute()
94  [ sym_1, wall_1, outlet_1, farfield_1 ] = Mesh_1.GetGroups()
95  try:
96    Mesh_1.ExportCGNS( r'../mesh_deformed_flow.cgns', 1, Mesh_1)
97    pass
98  except:
99    print('ExportCGNS() failed. Invalid file name?')
100 Mesh_1.RenumberNodes()
101 Mesh_1.RenumberElements()
102 [ sym_1, wall_1, outlet_1, farfield_1 ] = Mesh_1.GetGroups()
103 Mesh_1.RenumberNodes()
104 Mesh_1.RenumberElements()
105 [ sym_1, wall_1, outlet_1, farfield_1 ] = Mesh_1.GetGroups()
106 Sub_mesh_1 = Regular_1D.GetSubMesh()
107 Sub_mesh_2 = Regular_1D_1.GetSubMesh()
108 Sub_mesh_3 = Regular_1D_2.GetSubMesh()
109 Sub_mesh_4 = Regular_1D_3.GetSubMesh()
110 ## Set names of Mesh objects
111 smesh.SetName(Quadrangle_2D.GetAlgorithm(), 'Quadrangle_2D')
112 smesh.SetName(Regular_1D.GetAlgorithm(), 'Regular_1D')
113 smesh.SetName(Number_of_Segments_1, 'Number of Segments_1')
114 smesh.SetName(Number_of_Segments_2, 'Number of Segments_2')
115 smesh.SetName(Quadrangle_Parameters_1, 'Quadrangle Parameters_1')
116 smesh.SetName(Number_of_Segments_3, 'Number of Segments_3')
117 smesh.SetName(Number_of_Segments_4, 'Number of Segments_4')
118 smesh.SetName(Mesh_1.GetMesh(), 'Mesh_1')
119 smesh.SetName(sym_1, 'sym')
120 smesh.SetName(outlet_1, 'outlet')
121 smesh.SetName(wall_1, 'wall')
122 smesh.SetName(farfield_1, 'farfield')
123 smesh.SetName(Sub_mesh_4, 'Sub-mesh_4')
124 smesh.SetName(Sub_mesh_3, 'Sub-mesh_3')
125 smesh.SetName(Sub_mesh_2, 'Sub-mesh_2')
126 smesh.SetName(Sub_mesh_1, 'Sub-mesh_1')
127 exec(compile(open('../cfdmsh.py', 'rb').read(), '../cfdmsh.py', 'exec'))
128 ExportSU2File('Mesh_1', 'new_mesh.su2' )
```

Figure C.2: Second part of $su2\_mesher.py$ script

CURRICULUM VITAE

PERSONAL INFORMATION

Surname, Name: Çelik, Mutlu
Nationality: Turkish

EDUCATION

Degree	Institution	Year of Graduation
M.S.	METU	2022
B.S.	Bilkent University	2018
High School	Jale Tezer Private Anatolian High School	2013

PROFESSIONAL EXPERIENCE

Year	Place	Enrollment
03.2018-...	Roketsan Missiles Inc.	Aerothermal Design Engineer
01.2018-03.2018	Aselsan Inc.	Part-Time Thermal Design Engineer

PUBLICATIONS

International Conference Publications

Çelik M., Uğur Ö. and Eyi S., "Numerical Modeling of Hypersonic Air and Carbon Dioxide Flows in Thermochemical Non-equilibrium with SU2-NEMO Solver", International Conference on Flight Vehicles, Aerothermodynamics and Re-entry Missions Engineering (FAR), June 2022, Heilbronn/Germany.